Shape optimization and additive manufacturing: some new constraints and challenges

Grégoire Allaire[1], Charles Dapogny[2], Rafael Estevez[3], Alexis Faure[3], and Georgios Michailidis[3]

[1] CMAP, UMR 7641 École Polytechnique, Palaiseau, France
[2] CNRS & Laboratoire Jean Kuntzmann, Université Grenoble-Alpes, Grenoble, France
[3] SiMaP, Université Grenoble-Alpes, Grenoble, France

13th June, 2019

Foreword: shape optimization in the industrial context

- Shape and topology optimization techniques have aroused a tremendous enthusiasm within the engineering and industrial communities.
- One drawback of these methods is that the optimized designs are often too complicated to be constructed by traditional methods such as milling or casting.
- The recent headway made by additive manufacturing methods allow to assemble structures with a high degree of complexity...
- ... But these techniques raise new constraints about the manufactured components.

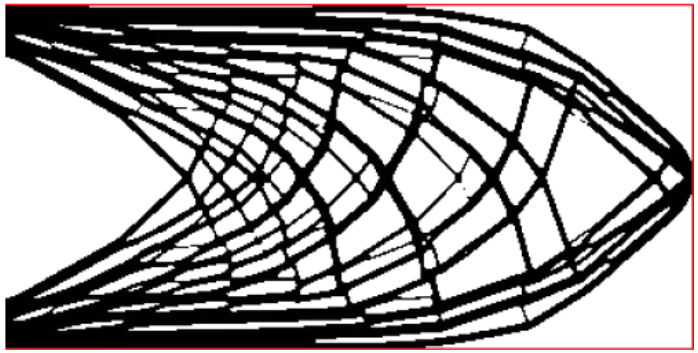

Typical 'truss' designs resulting from shape and topology optimization processes.

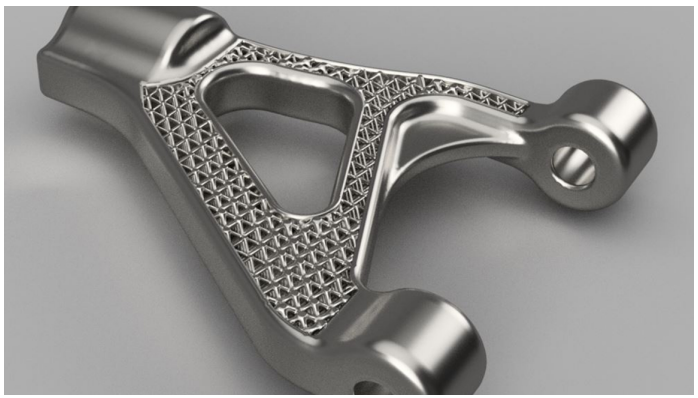

Part produced with an additive manufacturing method (from http://www.autodesk.com/).

1. Additive manufacturing techniques: assets and drawbacks
   - Additive manufacturing in a nutshell
   - The overhang issue
   - Anisotropy of the effective material properties
2. The structural optimization setting
3. Mechanical constraints for the presence of overhangs
   - The 'naive', geometric attempt and the 'dripping' effect
   - Presentation of the mechanical constraint
   - Numerical examples
4. A simple model for the material properties of parts assembled by additive techniques
   - A few words about the signed distance function
   - Different patterns for printing shapes
   - Numerical examples

Additive manufacturing in a nutshell (I)

- All the additive manufacturing processes begin with a slicing stage: the input shape is decomposed into a series of horizontal layers.
- These $2d$ layers are built one on top of the other according to the selected technology.

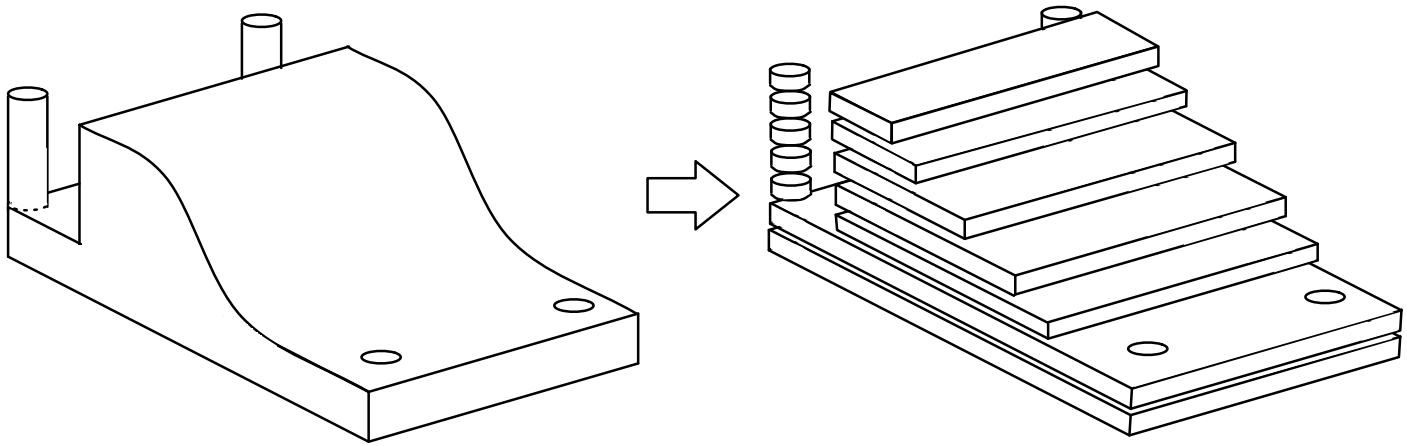

Sketch of the slicing procedure, initiating any additive manufacturing process.

- In principle, additive manufacturing technologies make it possible to construct arbitrarily complex shapes.

Additive manufacturing in a nutshell (II)

Two popular additive manufacturing technologies are:

- Material extrusion methods (e.g. FDM): they act by direct deposition of rasters of a molten filament. Such methods are often used to process plastic (ABS).
- Powder bed fusion methods (e.g. EBM, SLS), which are generally used to process metals. Each $2d$ layer is assembled by spreading metallic powder within the build chamber, then binding the grains together with a laser.

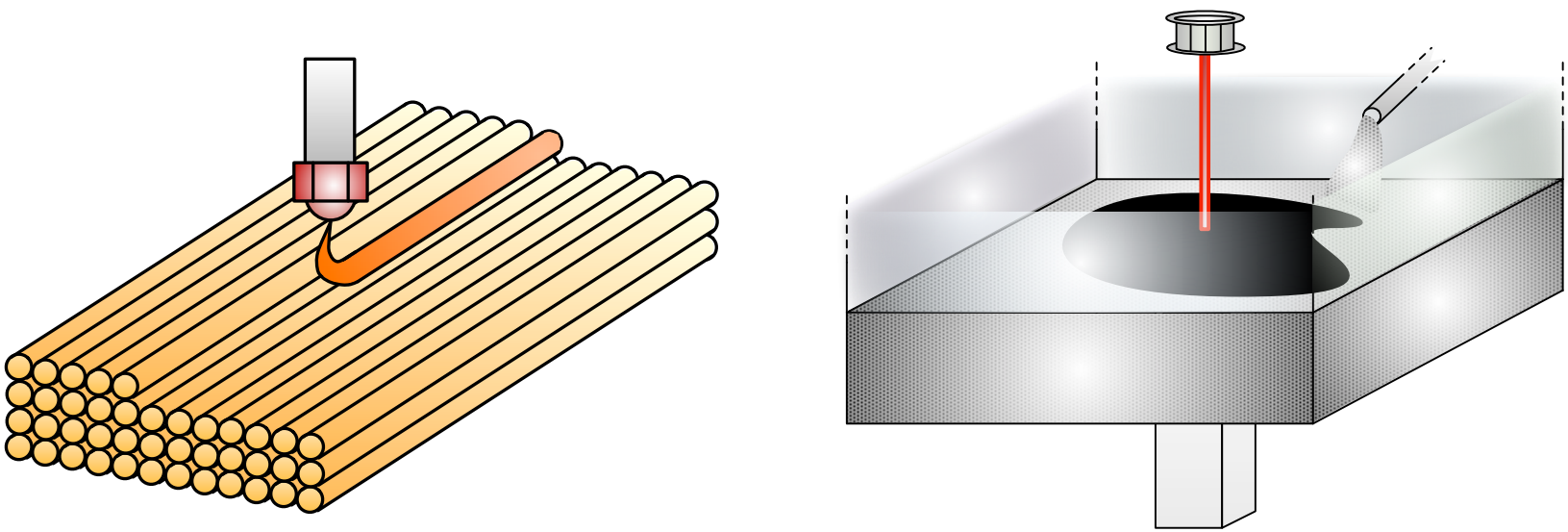

Sketch of the (left) FDM and (right) EBM additive manufacturing processes.

Additive manufacturing techniques in a nutshell (III)

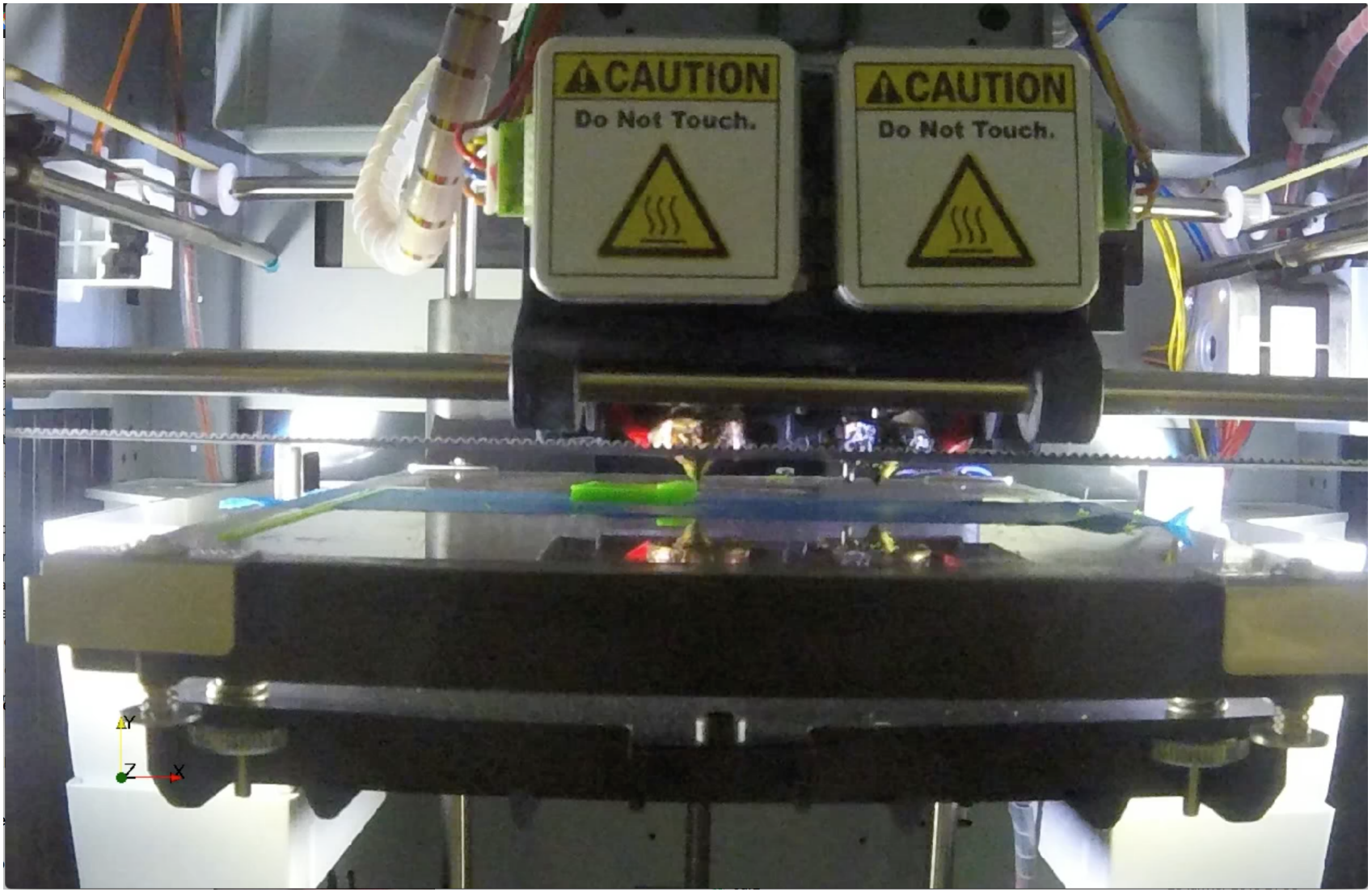

An FDM machine tool in action.

The overhang issue (I)

All additive manufacturing technologies experience trouble when assembling shapes with large overhangs, i.e. regions hanging over void.

- In the case of FDM processes, this amounts to assembling over void.
- In the case of powder-bed methods, the rapid melting then solidification of the powder induces residual stress, especially in regions unanchored to the lower structure. This may cause warpage of such parts upon cooling.

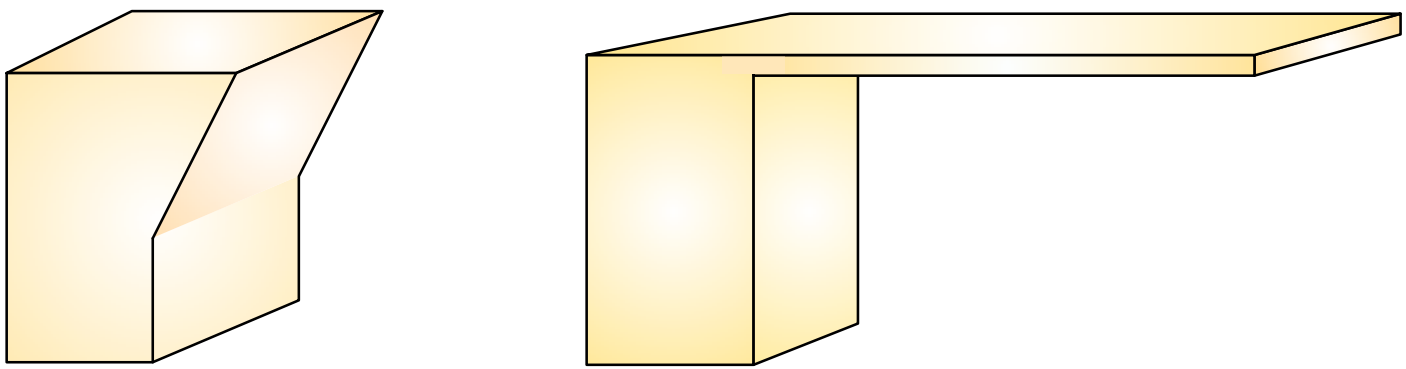

(Left) short overhang; support from the lower structure is sufficient to guarantee manufacturability; (right) large overhang.

The overhang issue (II)

- The most common strategy to deal with overhangs is to erect a sacrificial scaffold structure alongside the construction of the shape [DuHeLe].
- This scaffold structure has to be removed as a post-processing, which is costly and cumbersome.

$\Rightarrow$ Need to optimize designs so that they are overhang-free.

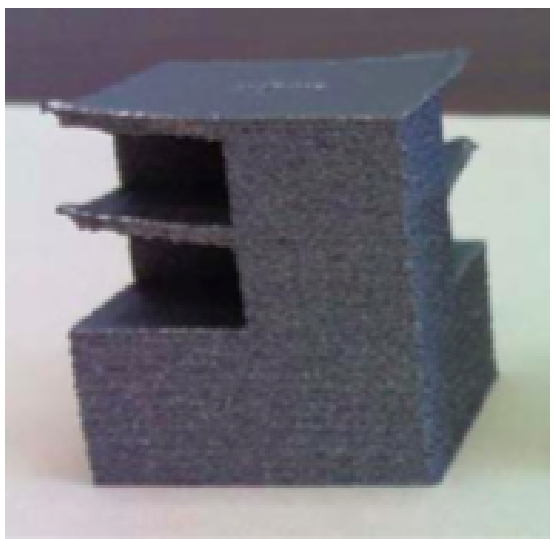

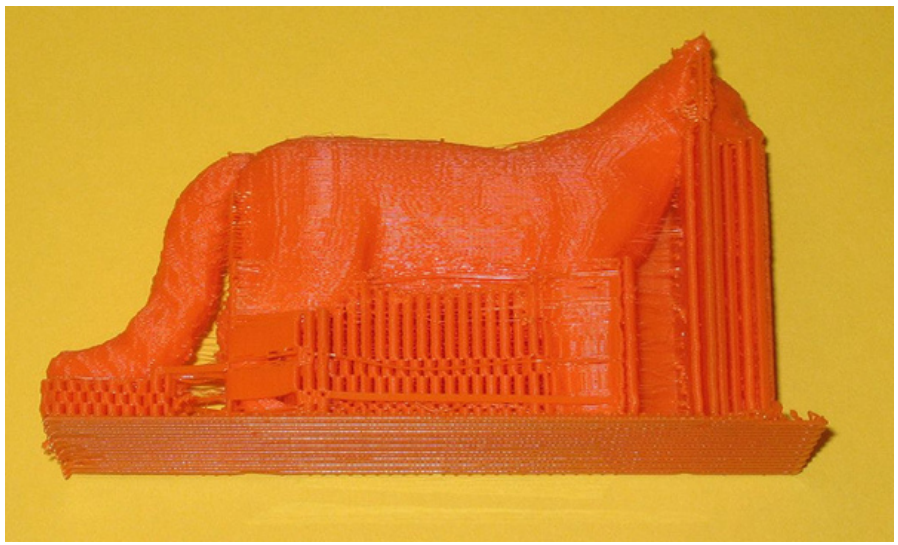

(Left) Warpage caused by residual constraints in an EBM assembly (from [CheLuChou]), (right) scaffold structure in the construction of a part (from `https://hyrulefoundry.wordpress.com/`*).*

Anisotropy of the effective material properties (I)

- The observed physical properties of the assembled materials (resistance to traction, to shear, etc.) do not match those predicted by theory.
- The main reason is that regions that are melted and solidify together present stronger bonds than those that cool apart from one another.
- The effective material properties of structures assembled by additive manufacturing are often anisotropic: they mainly depend on the pattern used for assembling each 2d layer... which may depend on the shape itself!
- It is a crucial challenge in engineering to model and incorporate this peculiar material behavior into the design optimization process.

Anisotropy of the effective material properties (II)

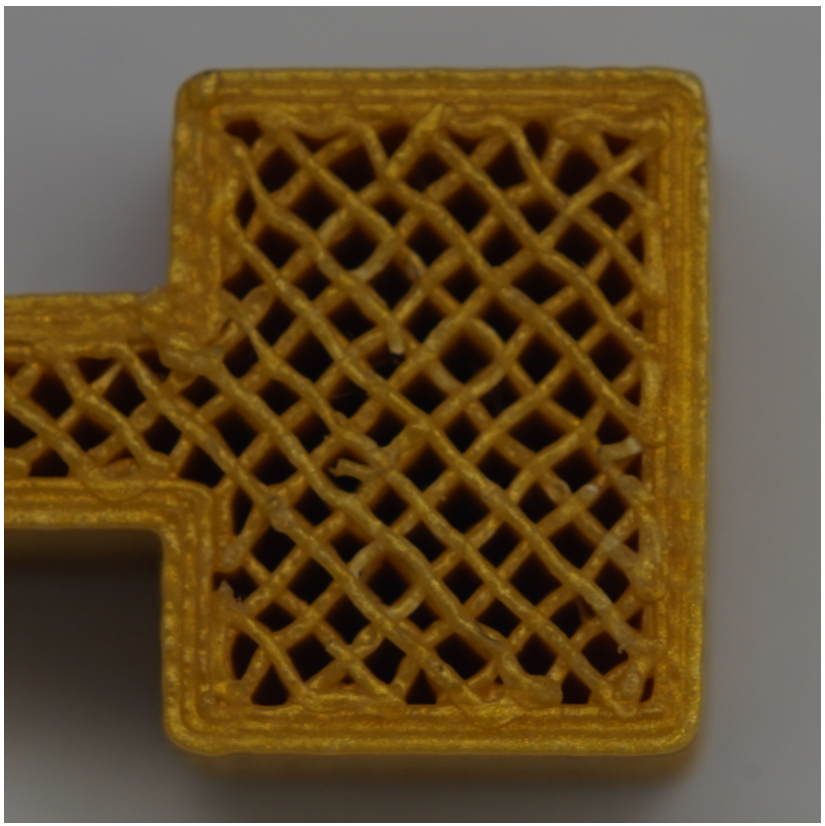

(Left) One device printed by starting with the contour, then using an infill pattern; (right) one part printed by following its contour offsets.

Shape optimization of linear elastic shapes

In the context of its final use, a shape is a bounded domain $\Omega \subset \mathbb{R}^d$, which is

- fixed on a part Γ_D of its boundary,
- submitted to surface loads f, applied on $\Gamma_N \subset \partial\Omega$, $\Gamma_D \cap \Gamma_N = \emptyset$.

The displacement vector field $u_\Omega : \Omega \to \mathbb{R}^d$ is governed by the linear elasticity system:

$$\begin{cases} -\mathrm{div}(Ae(u_\Omega)) &= 0 & \text{in } \Omega \\ u_\Omega &= 0 & \text{on } \Gamma_D \\ Ae(u_\Omega)n &= f & \text{on } \Gamma_N \\ Ae(u_\Omega)n &= 0 & \text{on } \Gamma \end{cases},$$

where $e(u) = \frac{1}{2}(\nabla u^T + \nabla u)$ is the strain tensor.

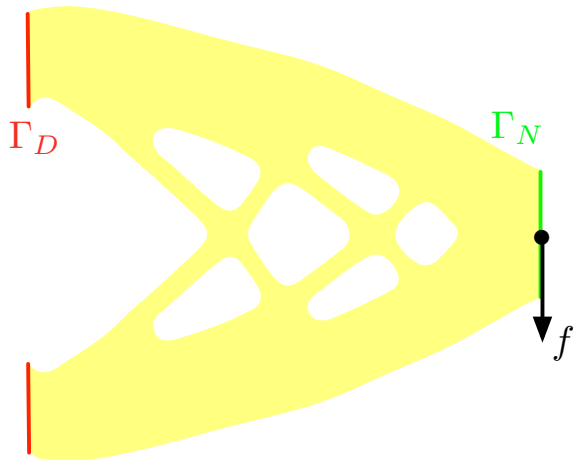

A 'Cantilever'

The deformed cantilever

The (isotropic) Hooke's tensor

The Hooke's law A of an isotropic material reads:

$$\forall e \in \mathcal{S}_d(\mathbb{R}), \quad Ae = 2\mu e + \lambda \mathrm{tr}(e) I.$$

where the Lamé parameters λ, μ are related to the more physical quantities E and ν:

$$\mu = \frac{E}{2(1+\nu)}, \text{ and } \lambda = \frac{E\nu}{(1+\nu)(1+\nu(1-d))}.$$

- The Young's modulus

  $$E = \sigma / L$$

  measures the resistance to deformation under traction;

- The Poisson's ratio

  $$\nu = -\ell / L$$

  accounts for the relative transverse displacement for a given longitudinal deformation.

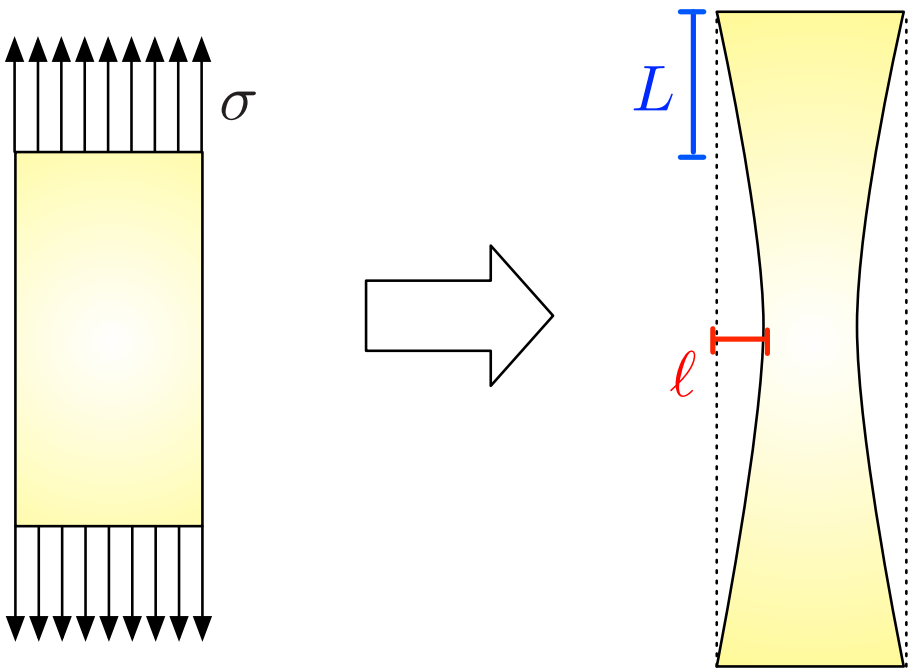

The (anisotropic) Hooke's tensor

- Anisotropic materials have different physical properties (i.e. Young's modulus, Poisson's ratio, etc.) depending on the direction.
- The Hooke's tensor A is a general mapping $A : \mathcal{S}_d(\mathbb{R}) \to \mathcal{S}_d(\mathbb{R})$.
- Most materials of interest are orthotropic: their properties have d principal directions: they have one Young's modulus in each principal direction, two Poisson's ratios and one shear modulus for each pair of directions.

Fiber-reinforced concrete and wood are examples of orthotropic materials.

The shape optimization problem

The shape optimization problem of interest reads:

$$\min_{\mathcal{U}_{\mathrm{ad}}} J(\Omega), \text{ s.t. } P(\Omega) \leq \alpha,$$

in which

- $\mathcal{U}_{\mathrm{ad}}$ is a set of (smooth) admissible shapes,
- The objective function $J(\Omega)$ is the structural compliance of shapes:

$$J(\Omega) = \int_{\Omega} Ae(u_\Omega) : e(u_\Omega)\, dx = \int_{\Gamma_N} f \cdot u_\Omega\, ds,$$

- The constraint $P(\Omega)$ enforces e.g. the constructibility by additive manufacturing processes,
- Other constraints may be added to the problem, e.g. on the volume $\mathrm{Vol}(\Omega)$ of shapes.

Differentiation with respect to the domain: Hadamard's method

Hadamard's boundary variation method describes variations of a reference, Lipschitz domain Ω of the form:

$$\Omega \to \Omega_\theta := (\mathrm{Id} + \theta)(\Omega),$$

for 'small' $\theta \in W^{1,\infty}\left(\mathbb{R}^d, \mathbb{R}^d\right)$.

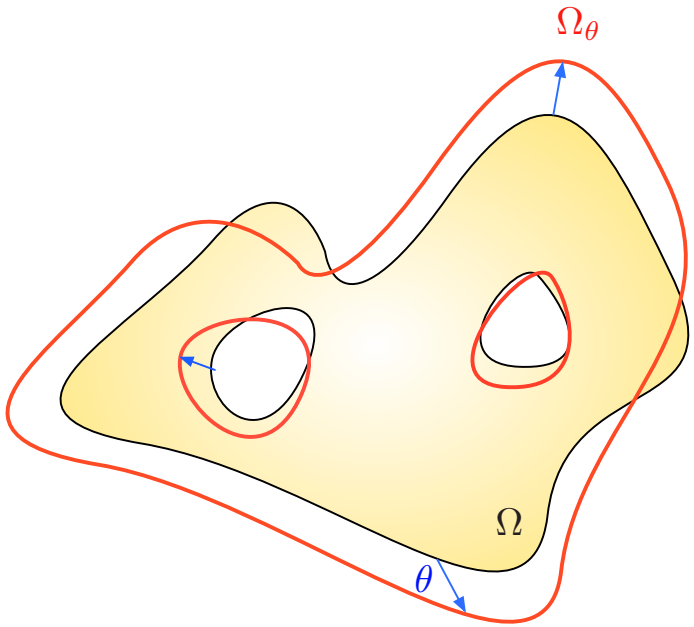

Definition 1.

Given a smooth domain Ω, a function $J(\Omega)$ of the domain is shape differentiable at Ω if the function

$$W^{1,\infty}(\mathbb{R}^d, \mathbb{R}^d) \ni \theta \mapsto J(\Omega_\theta)$$

is Fréchet-differentiable at 0, i.e. the following expansion holds around 0:

$$J(\Omega_\theta) = J(\Omega) + J'(\Omega)(\theta) + o\left(||\theta||_{W^{1,\infty}(\mathbb{R}^d,\mathbb{R}^d)}\right).$$

Techniques from optimal control theory make it possible to calculate shape derivatives; in the case of 'many' functionals of the domain $J(\Omega)$, the shape derivative has the particular structure:

$$J'(\Omega)(\theta) = \int_\Gamma v_\Omega \, \theta \cdot n \, ds,$$

where v_Ω is a scalar field depending on u_Ω, and possibly on an adjoint state p_Ω.

Example: If the objective function

$$J(\Omega) = \int_{\Gamma_N} f \cdot u_\Omega \, ds$$

is the compliance, $v_\Omega = -Ae(u_\Omega) : e(u_\Omega)$ is the (negative) elastic energy density.

The generic algorithm

This shape gradient provides a natural descent direction for $J(\Omega)$: *for instance*, defining θ as

$$\theta = -v_\Omega n$$

yields, for $t > 0$ sufficiently small (*to be found numerically*):

$$J((\mathrm{Id} + t\theta)(\Omega)) = J(\Omega) - t\int_\Gamma v_\Omega^2 ds + o(t) < J(\Omega)$$

Gradient algorithm: For $n = 0, \ldots$ until convergence,

1. Compute the solution u_{Ω^n} (and p_{Ω^n}) of the elasticity system on Ω^n.
2. Compute the shape gradient $J'(\Omega^n)$ thanks to the previous formula, and infer a descent direction θ^n for the cost functional.
3. Advect the shape Ω^n according to θ^n, so as to get $\Omega^{n+1} := (\mathrm{Id} + \theta^n)(\Omega^n)$.

In practice Shapes and their deformations are accounted for by the level set method [AlJouToa].

The 'naive', geometric attempt (I)

- Most approaches in the literature rely on the angle between $\partial\Omega$ and the (vertical) build direction to detect and penalize overhangs.
- An intuitive approach relies on anisotropic perimeter functionals of the form:

$$P_g(\Omega) = \int_{\partial\Omega} \varphi(n_\Omega)\, ds, \text{ where } \varphi : \mathbb{R}^d \to \mathbb{R} \text{ is given.}$$

Example The choice $\varphi_a(n) := (n \cdot e_d + \cos\nu)_-^2$, where $(s)_- := \min(s, 0)$, penalizes regions of $\partial\Omega$ where the angle $n \cdot (-e_d)$ is smaller than a threshold ν.

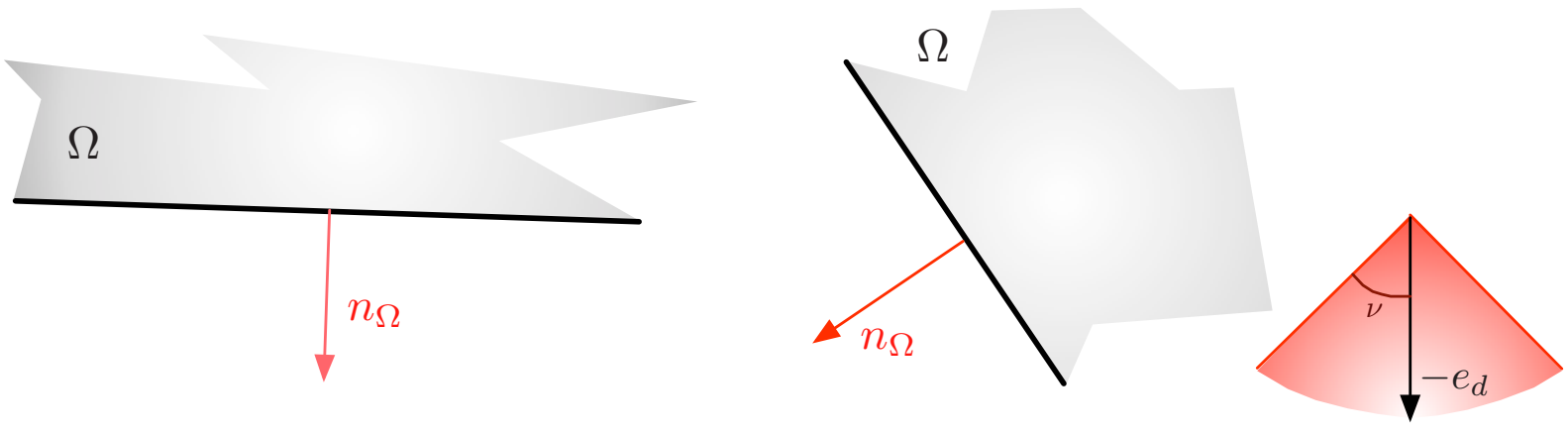

Parts of $\partial\Omega$ (left) violating and (right) satisfying the angle-based criterion.

The 'naive', geometric attempt (II)

Proposition 1.

The functional $P_g(\Omega)$ is shape differentiable at any admissible shape $\Omega \in \mathcal{U}_{\mathrm{ad}}$, and its shape derivative reads:

$$P_g'(\Omega)(\theta) = \int_\Gamma \kappa\, \varphi(n)\, \theta \cdot n \, ds - \int_\Gamma \nabla(\varphi(n)) \cdot \nabla_{\partial\Omega}(\theta \cdot n)\, ds,$$

where $\nabla_{\partial\Omega}\psi := \nabla\psi - (\nabla\psi \cdot n)n$ is the tangential gradient of a smooth enough function $\psi : \partial\Omega \to \mathbb{R}$.

- Unfortunately, this approach gives unsatisfactory results.
- We propose instead a general idea for modeling overhang constraints, which appeals to their mechanical origin.

Geometric constraints; the 'dripping effect' (I)

We consider the two-dimensional MBB Beam example.

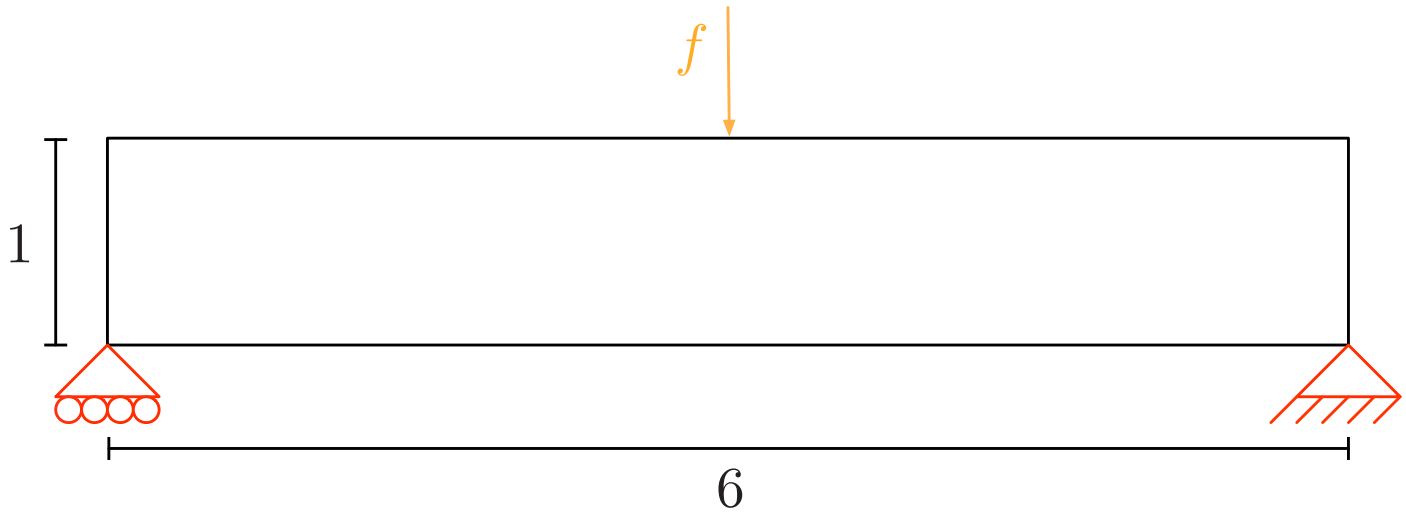

Setting of the two-dimensional MBB beam example.

We first solve the compliance minimization problem:

$$\begin{aligned} \min_{\Omega} \quad & J(\Omega), \\ \text{s.t.} \quad & \mathrm{Vol}(\Omega) \leq \alpha_v \mathrm{Vol}(D). \end{aligned}$$

Geometric constraints; the 'dripping effect' (II)

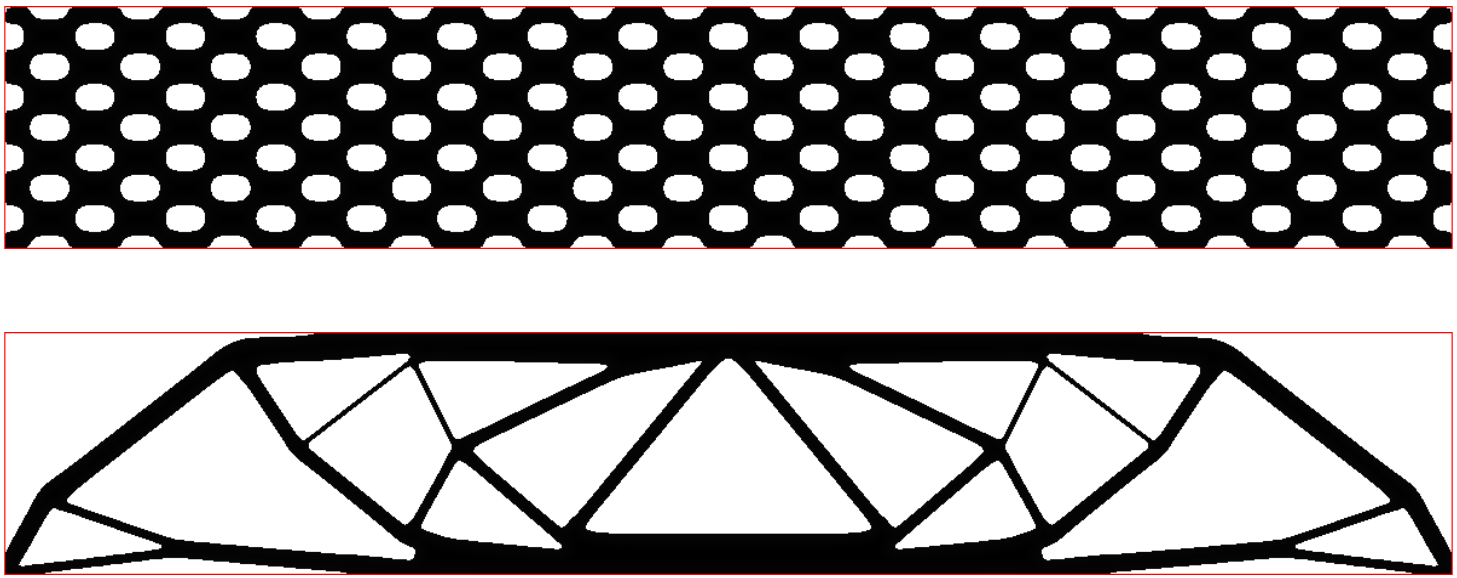

(Top) initial shape Ω_0 and (bottom) optimized shape Ω^* for compliance minimization in the two-dimensional MBB Beam example.

The optimized shape Ω^* presents large nearly horizontal bars which are very important for the structural performance.

Geometric constraints; the 'dripping effect' (III)

To help in removing these overhangs, we rather solve the problem:

$$\begin{aligned} \min_{\Omega} \quad & (1-\alpha_g)\frac{J(\Omega)}{J(\Omega^*)} + \alpha_g \frac{P_g(\Omega)}{P_g(\Omega^*)}, \\ \text{s.t.} \quad & \mathrm{Vol}(\Omega) \leq \alpha_v \mathrm{Vol}(D). \end{aligned}$$

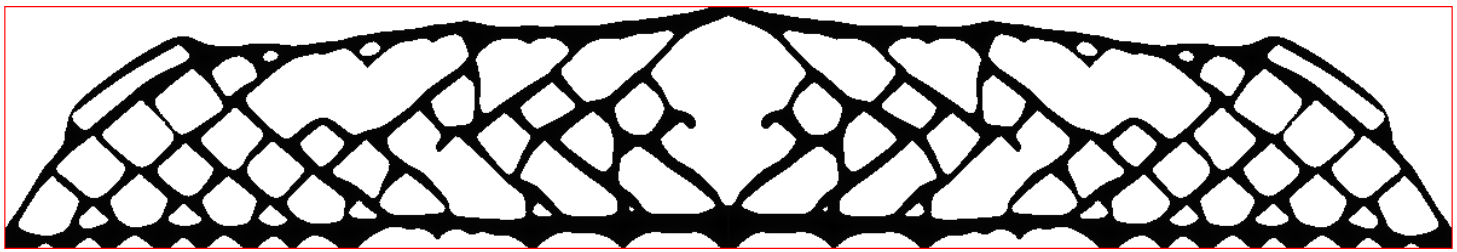

Optimized shape using $\alpha_g = 0.5$.

The shape develops an oscillatory boundary so that:

- The angle requirement is (approximately) satisfied,
- The structural performance is not too much altered: the large bars connecting loads to anchor points have not disappeared.

Definition of the mechanical constraint (I)

The mechanical constraint $P(\Omega)$ relies on the physical behavior of the shape at each stage of its construction.

- Ω is enclosed in the build chamber $D = S \times (0, H)$, where $S \subset \mathbb{R}^{d-1}$,
- $\Omega_h := \{x = (x_1, ..., x_d) \in \Omega,\ x_d < h\}$ is the intermediate shape at height h.
- The boundary $\partial\Omega_h$ is decomposed as $\partial\Omega_h = \Gamma_0 \cup \Gamma_h^u \cup \Gamma_h^l$, where
  - $\Gamma_0 = \{x \in \partial\Omega_h,\ x_d = 0\}$ is the contact region between Ω and the build table,
  - $\Gamma_h^u = \{x \in \partial\Omega_h,\ x_d = h\}$ is the upper side of Ω_h,
  - $\Gamma_h^l = \partial\Omega_h \setminus (\overline{\Gamma_0} \cup \overline{\Gamma_h^u})$ is the lateral surface.

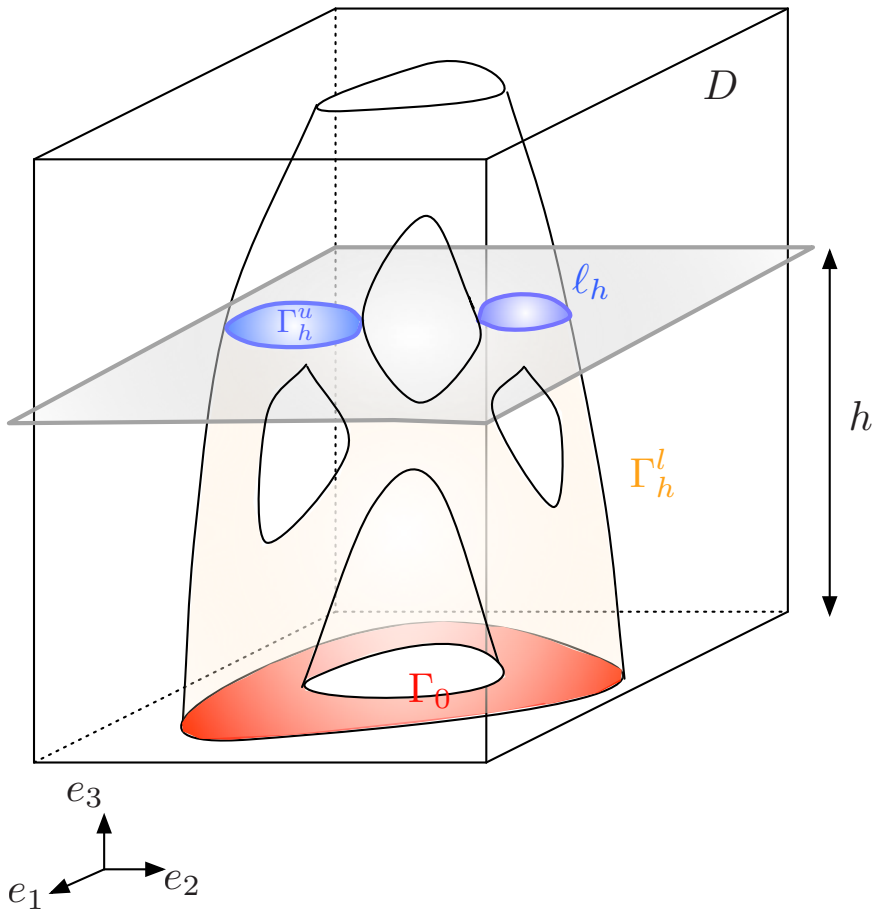

Definition of the mechanical constraint (II)

- Each intermediate shape Ω_h is only subjected to gravity effects $g \in H^1(\mathbb{R}^d)^d$. The elastic displacement of Ω_h satisfies:

$$\begin{cases} -\mathrm{div}(Ae(u^c_{\Omega_h})) = g & \text{in } \Omega_h, \\ u^c_{\Omega_h} = 0 & \text{on } \Gamma_0, \\ Ae(u^c_{\Omega_h})n = 0 & \text{on } \Gamma^l_h \cup \Gamma^u_h. \end{cases}$$

- The self-weight of each intermediate shape Ω_h is:

$$c_{\Omega_h} := \int_{\Omega_h} Ae(u^c_{\Omega_h}) : e(u^c_{\Omega_h})\, dx = \int_{\Omega_h} g \cdot u^c_{\Omega_h}\, dx.$$

- The (self-weight) manufacturing compliance of a final shape Ω aggregates the self weights of all its intermediate shapes:

$$P_{\mathrm{sw}}(\Omega) = \int_0^H j(c_{\Omega_h})\, dh,$$

where $j : \mathbb{R} \to \mathbb{R}$ is a smooth function.

Other models

Other models may be used for the physical behavior of intermediate shapes Ω_h. For instance,

- The definition of $u^c_{\Omega_h}$ could be replaced by:

$$\begin{cases} -\mathrm{div}(Ae(u^a_{\Omega_h})) = g_h & \text{in } \Omega_h, \\ u^a_{\Omega_h} = 0 & \text{on } \Gamma_0, \\ Ae(u^a_{\Omega_h})n = 0 & \text{on } \Gamma^l_h, \\ Ae(u^a_{\Omega_h})n = 0 & \text{on } \Gamma^u_h, \end{cases} \quad \text{where } g_h(x) = \begin{cases} g & \text{if } x_d \in (h-\delta, h), \\ 0 & \text{otherwise,} \end{cases}$$

  is an artificial force acting on the upper side of Ω_h. As we shall see, this formulation is better at penalizing perfectly horizontal parts hanging over void.

- The mechanical constraint $P(\Omega)$ could involve the solution v_{Ω_h} to a thermal cooling problem posed on Ω_h, to model e.g. residual stresses in the final shape Ω; see [AlJak].

Shape derivative of the manufacturing compliance (I)

- We consider a fixed shape $\Omega \in \mathcal{U}_{\mathrm{ad}}$.
- Perturbations θ are confined to a class X^k of vector fields of class $\mathcal{C}^k$, which identically vanish near the 'flat regions' of $\partial\Omega$.

Theorem 2.

The manufacturing compliance $P_{\mathrm{sw}}(\Omega)$ is shape differentiable at Ω, in the sense that the mapping $\theta \mapsto P_{\mathrm{sw}}(\Omega_\theta)$, from X^k into $\mathbb{R}$ is differentiable for $k \geq 1$; moreover,

$$\forall \theta \in X^k, \quad P'_{\mathrm{sw}}(\Omega)(\theta) = \int_{\partial\Omega \setminus \overline{\Gamma_0}} \mathcal{D}_\Omega \, \theta \cdot n \, ds,$$

where the integrand factor $\mathcal{D}_\Omega$ is defined, for a.e. $x \in \partial\Omega \setminus \overline{\Gamma_0}$, by:

$$\mathcal{D}_\Omega(x) = \int_{x_d}^{H} j'(c_{\Omega_h}) \left(2g \cdot u^c_{\Omega_h} - Ae(u^c_{\Omega_h}) : e(u^c_{\Omega_h})\right)(x) \, dh.$$

Mechanical approach: the manufacturing compliance (I)

Still in the setting of the two-dimensional MBB Beam example,

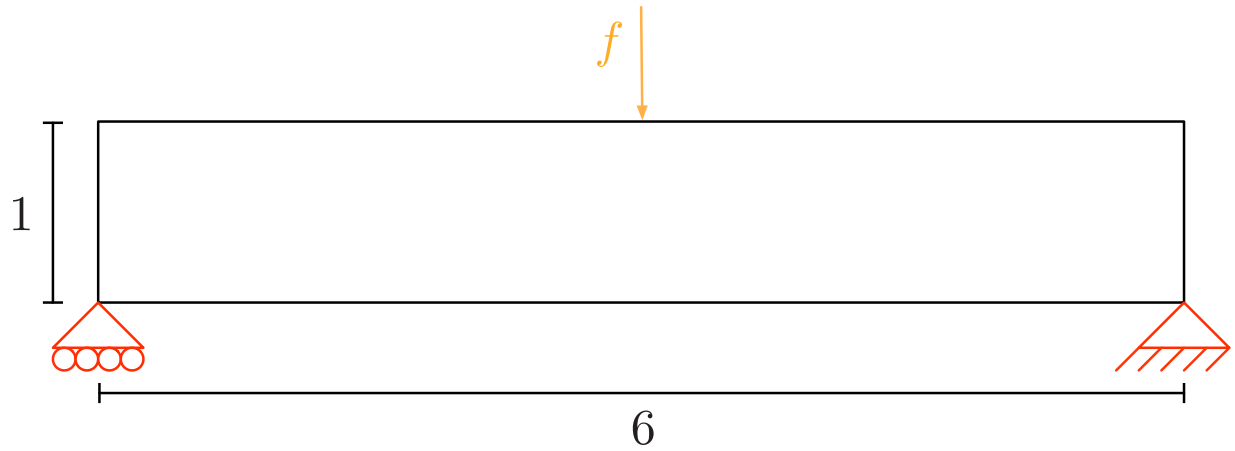

we now solve the constrained optimization problem:

$$\begin{aligned} \min_{\Omega} \quad & J(\Omega) \\ \text{s.t.} \quad & \mathrm{Vol}(\Omega) \leq \alpha_v \mathrm{Vol}(D), \\ & P_{\mathrm{sw}}(\Omega) \leq \alpha_c P_{\mathrm{sw}}(\Omega^*), \end{aligned}$$

where $\alpha_c \in [0, 1]$ is a user-defined tolerance, and Ω^* is the optimized shape for the compliance under volume constraint (without additive manufacturing constraint).

Mechanical approach: the manufacturing compliance (II)

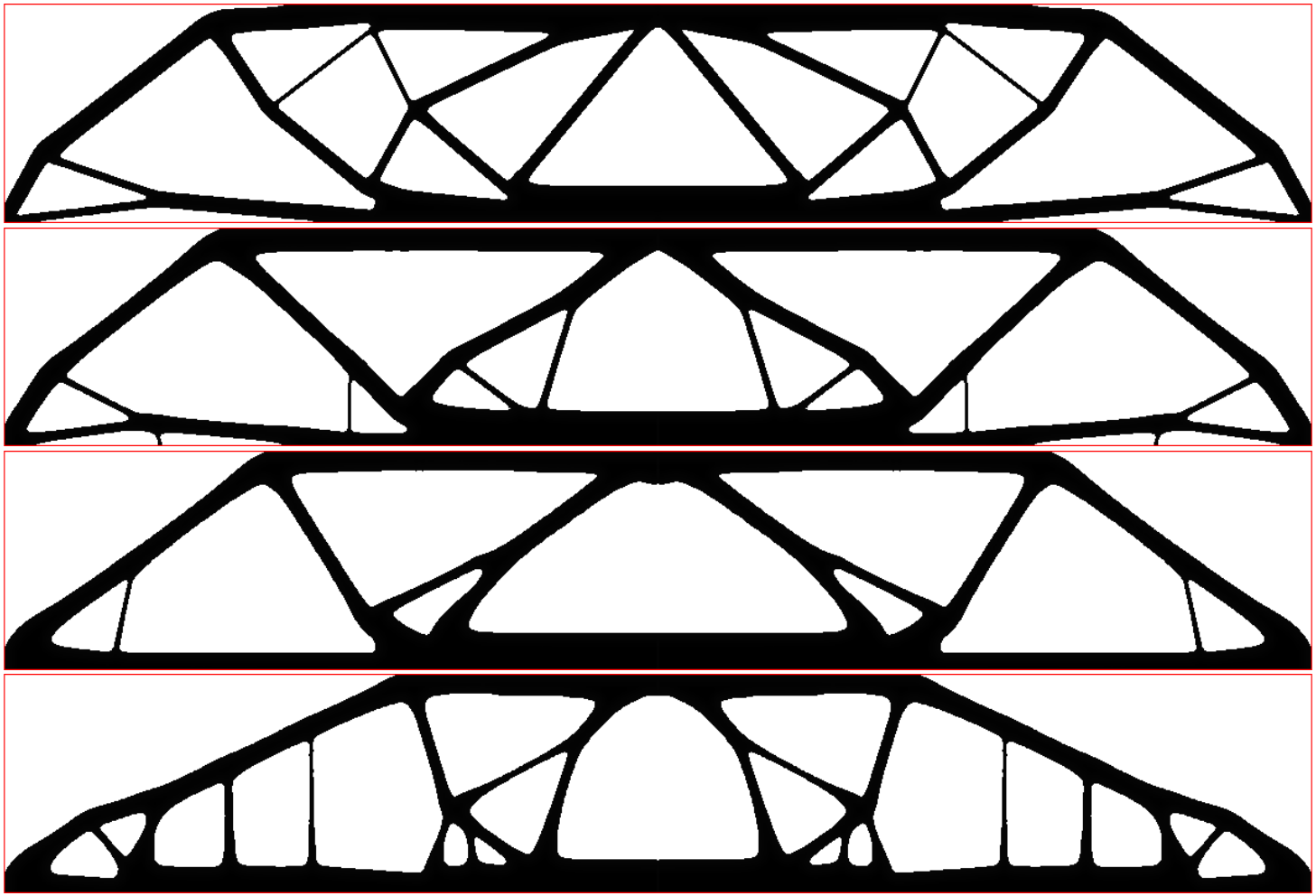

Optimized shapes for the two-dimensional MBB Beam example; (top) optimized shape Ω^**, without additive manufacturing constraints, and optimized shapes using parameters (from top to bottom)* $\alpha_c = 0.50$*,* $\alpha_c = 0.30$*, and* $\alpha_c = 0.10$*.*

Mechanical approach: the manufacturing compliance (III)

This new approach yields better results; yet, it raises two issues:

1. $P_{\mathrm{sw}}(\Omega)$ inherently favors structures whose lower part is stronger.
2. The optimized shapes still show large, completely horizontal overhangs. This is a flaw in the modelling of $P_{\mathrm{sw}}(\Omega)$, which assumes that each layer of material is assembled instantaneously.

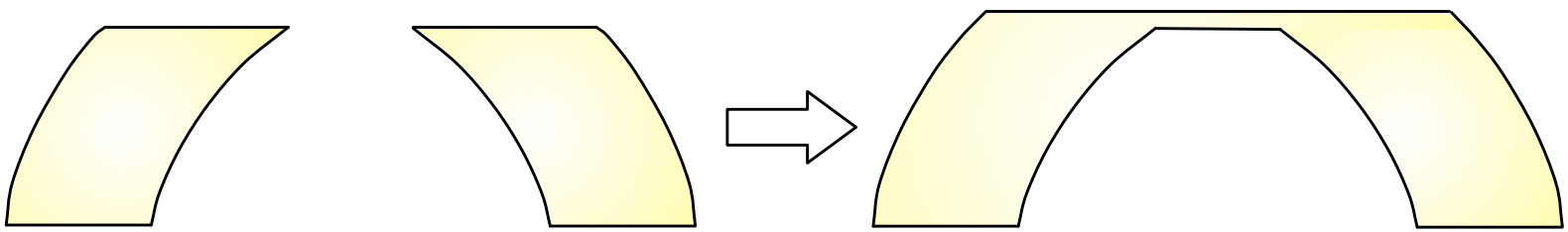

Completely flat overhangs are not so weak because of the instantaneous layer deposition assumption.

Mechanical approach: the modified manufacturing compliance (I)

We now solve:

$$\begin{array}{ll} \min\limits_{\Omega} & J(\Omega) \\ \text{s.t.} & \mathrm{Vol}(\Omega) \leq \alpha_v \mathrm{Vol}(D), \\ & P_{\mathrm{uw}}(\Omega) \leq \alpha_c P_{\mathrm{uw}}(\Omega^*), \end{array}$$

where the modified (upper weight) manufacturing compliance $P_{\mathrm{uw}}(\Omega)$ brings into plays elastic displacements of the intermediate shapes $u^a_{\Omega_h}$ involving an artificial load concentrated on their upper side:

$$\begin{cases} -\mathrm{div}(Ae(u^a_{\Omega_h})) = g_h & \text{in } \Omega_h, \\ u^a_{\Omega_h} = 0 & \text{on } \Gamma_0, \\ Ae(u^a_{\Omega_h})n = 0 & \text{on } \Gamma^l_h, \\ Ae(u^a_{\Omega_h})n = 0 & \text{on } \Gamma^u_h, \end{cases} \quad \text{where } g_h(x) = \begin{cases} g & \text{if } x_d \in (h-\delta, h), \\ 0 & \text{otherwise.} \end{cases}$$

Mechanical approach: the modified manufacturing compliance (II)

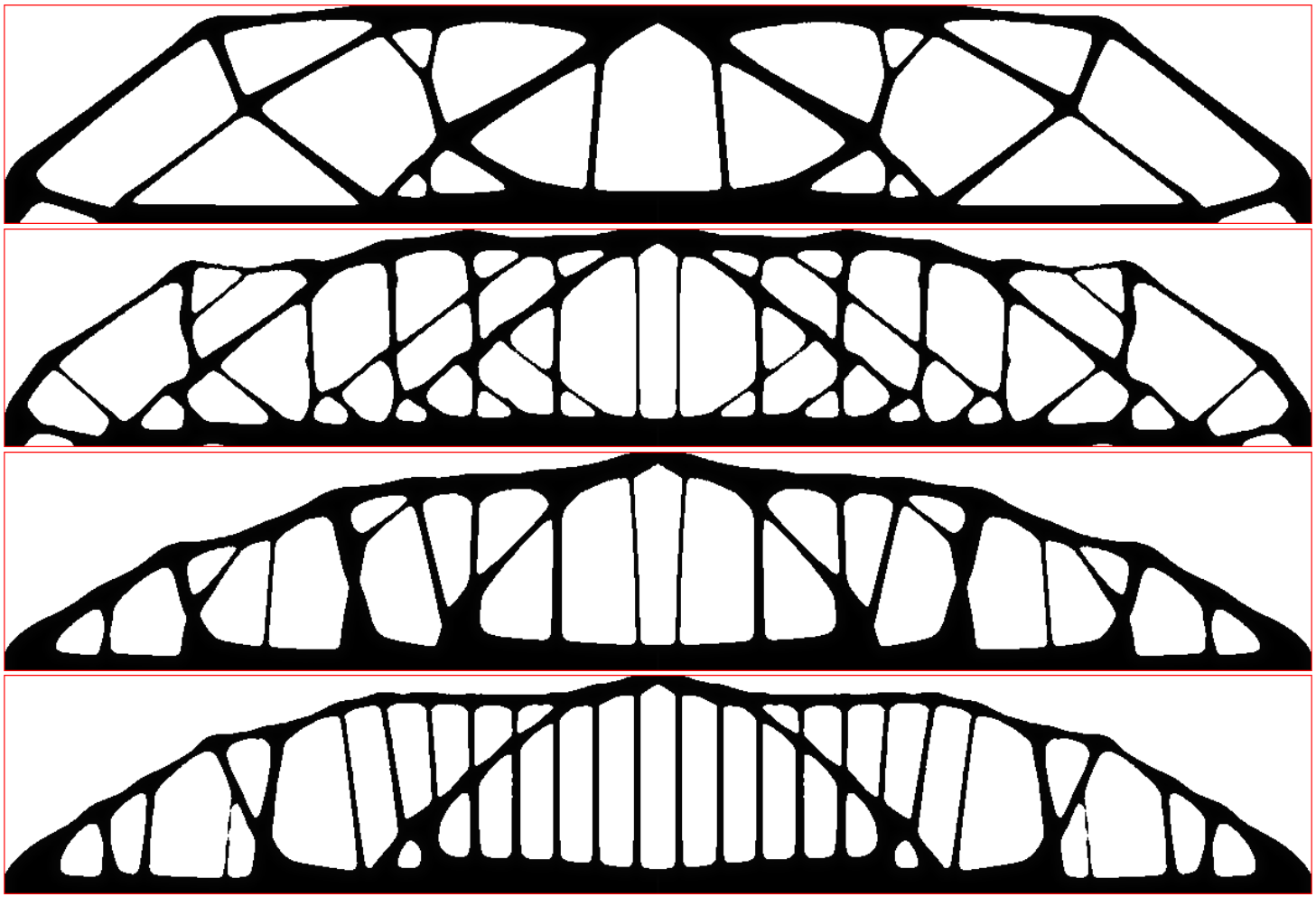

Optimized 2d MBB Beams obtained using the modified manufacturing compliance $P_{\mathrm{af}}(\Omega)$ *and parameters (from top to bottom)* $\alpha_c = 0.30$, $\alpha_c = 0.10$, $\alpha_c = 0.05$, *and* $\alpha_c = 0.03$.

Mechanical approach: the modified manufacturing compliance (III)

We now consider the design of a three-dimensional bridge.

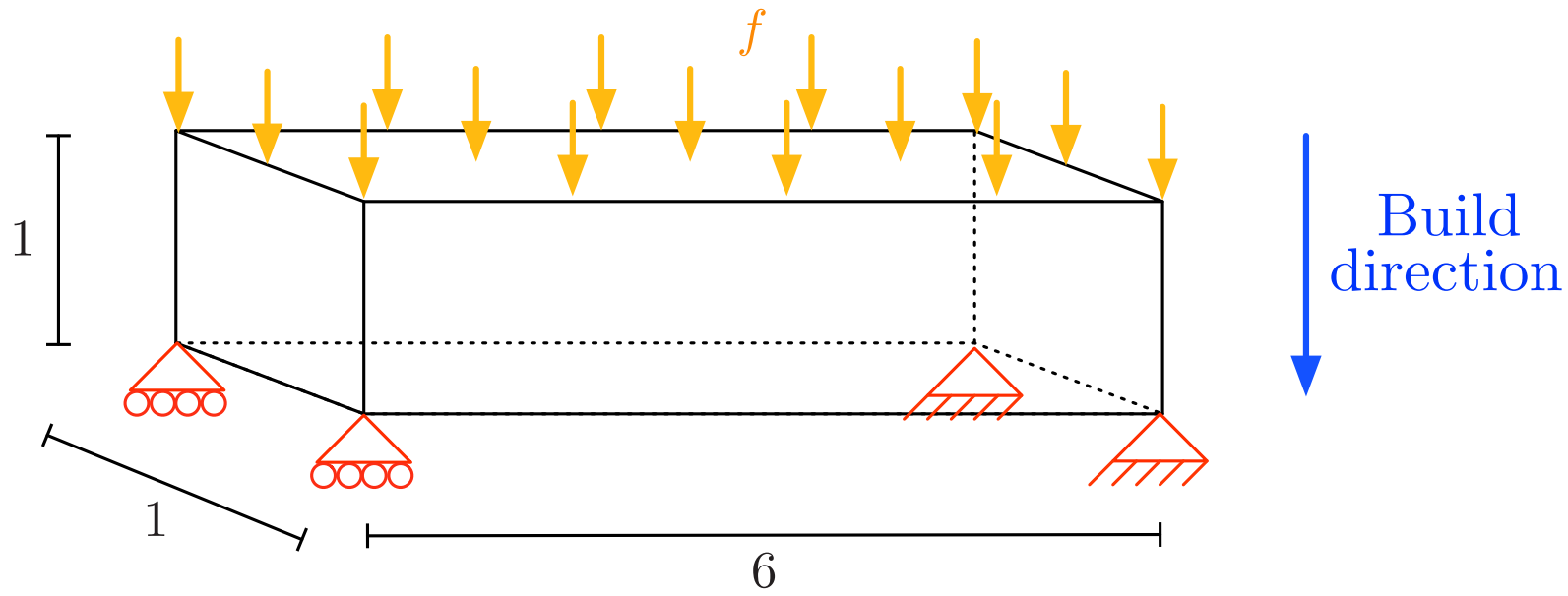

We solve the following shape optimization problem:

$$\begin{aligned} \min_{\Omega} \quad & \mathrm{Vol}(\Omega), \\ \text{s.t.} \quad & J(\Omega) \leq J(\Omega^*), \\ & P_{\mathrm{uw}}(\Omega) \leq \alpha_c P_{\mathrm{uw}}(\Omega^*). \end{aligned}$$

Mechanical approach: the modified manufacturing compliance (IV)

The optimized shape Ω^* without manufacturing shows several large overhangs.

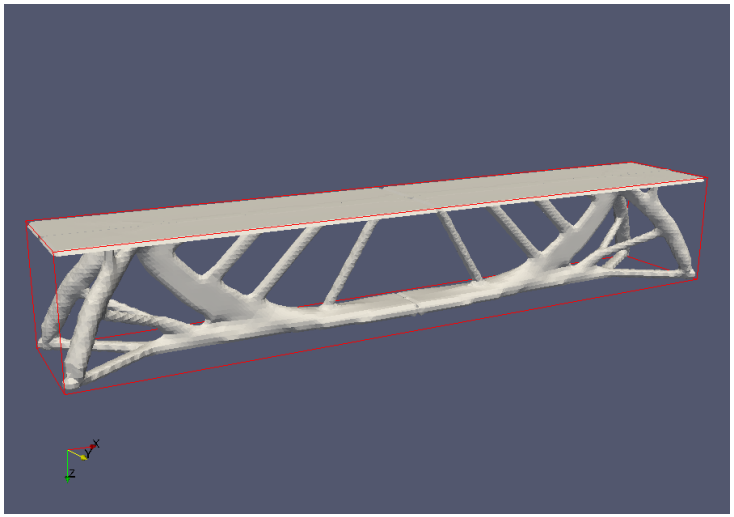

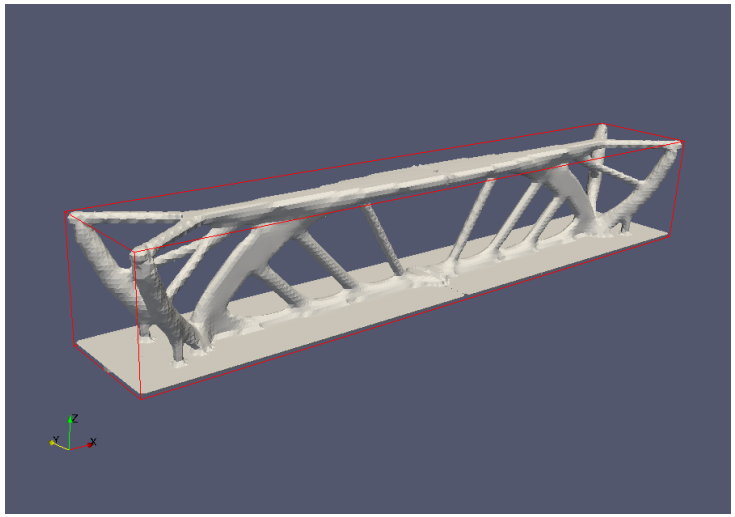

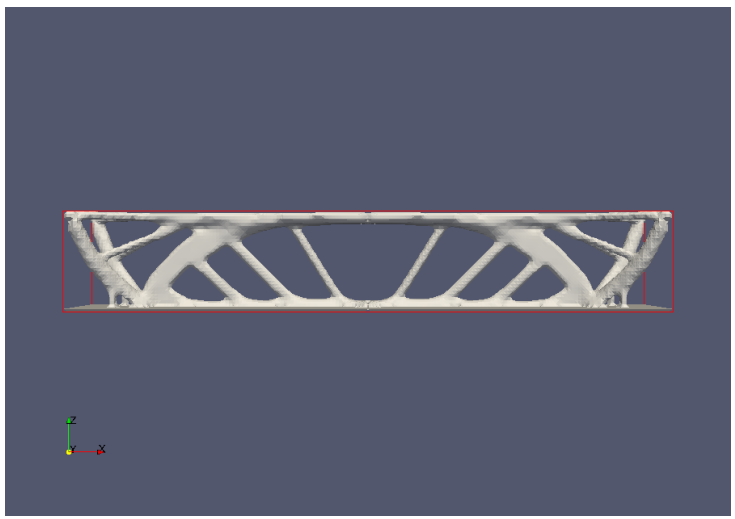

Different views of the unconstrained optimized shape Ω^*.

Mechanical approach: the modified manufacturing compliance (V)

Several small overhangs remain on the upper part of the optimized shape with the imposed manufacturing constraint $P_{\mathrm{uw}}(\Omega)$.

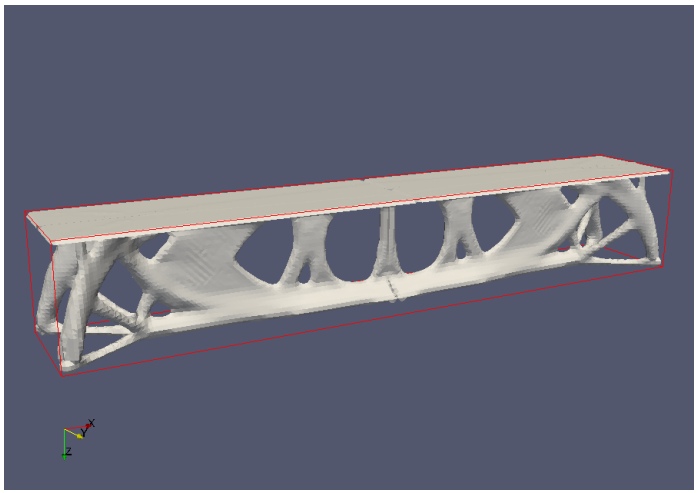

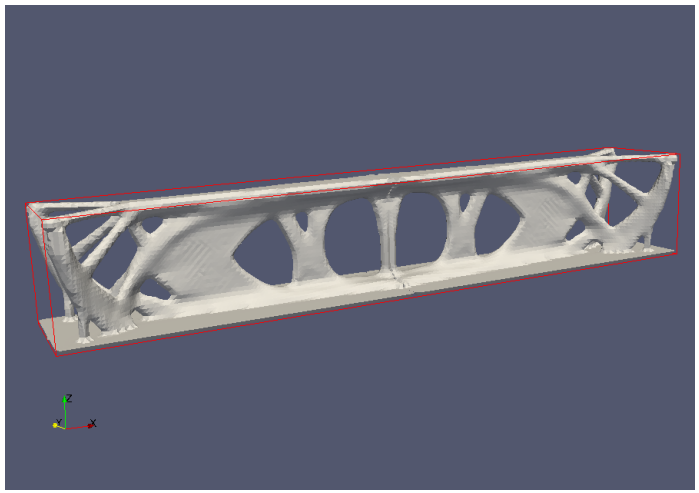

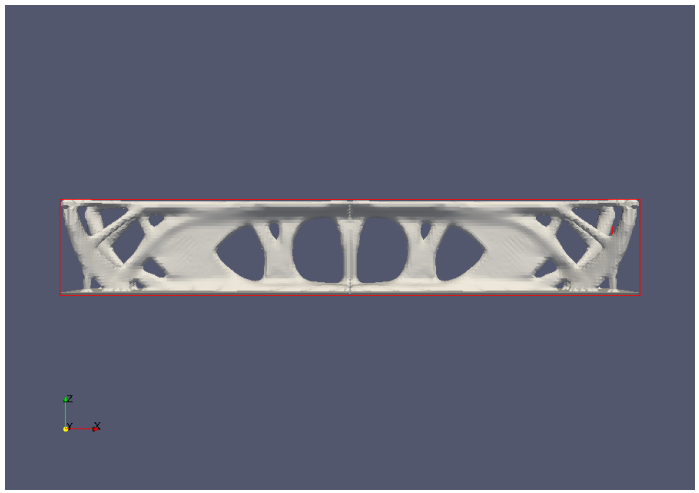

Different views of the optimized shape for $\alpha_c = 0.1$.

Effective material properties of additively assembled shapes

- The material properties are influenced by the path of the machine tool during the assembly of each 2d layer.
- Our study focuses on the 2d case: we model the material properties inside one 2d layer of a 'true' 3d shape.
- We propose models for the properties associated to two different printing patterns, but various different situations could be dealt with by similar means.
- Our constructions rely on the notion of signed distance function.

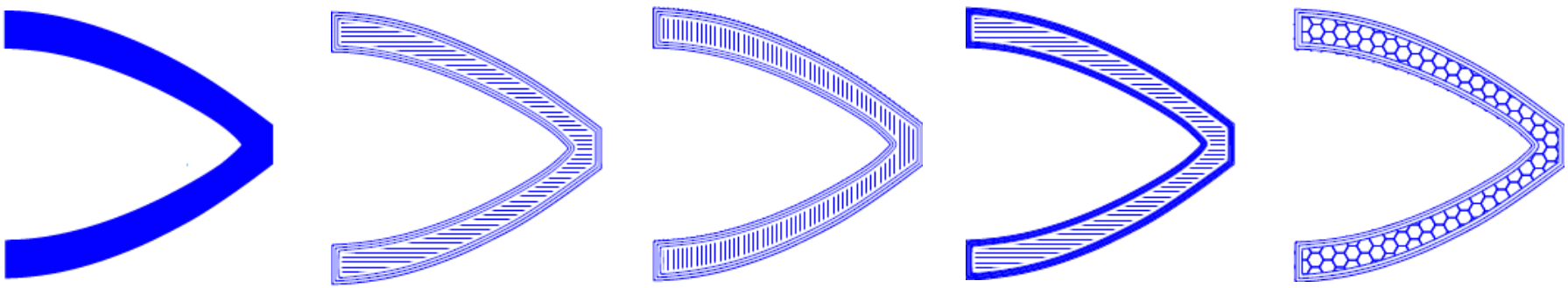

Several printing patterns for one 2d layer of a 3d structure.

Definition 2.

The signed distance function d_Ω *to a bounded domain* $\Omega \subset \mathbb{R}^d$ *is defined by:*

$$\forall x \in \mathbb{R}^d, \quad \begin{cases} -d(x, \partial\Omega) & \text{if } x \in \Omega \\ 0 & \text{if } x \in \partial\Omega \\ d(x, \partial\Omega) & \text{if } x \in {}^c\overline{\Omega} \end{cases},$$

where $d(x, \partial\Omega) = \min_{y \in \partial\Omega} |x - y|$ *is the usual Euclidean distance function to* $\partial\Omega$.

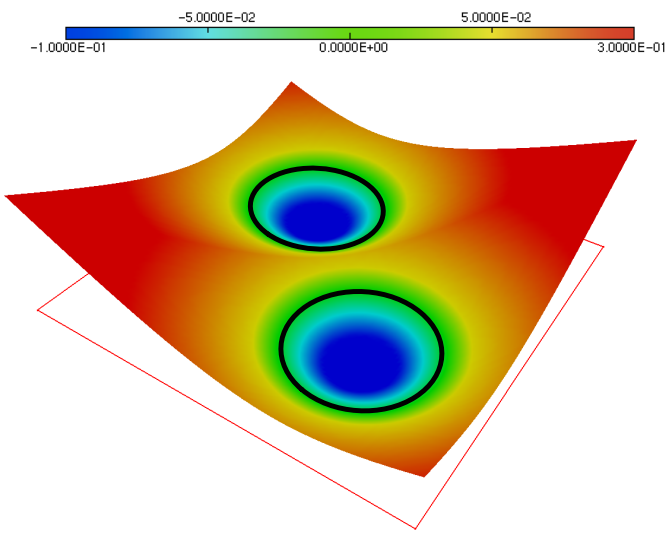

Graph of the signed distance function to a union of two disks (in black)

Definition 3.

Let $\Omega \subset \mathbb{R}^d$ be a Lipschitz, bounded open set;

- *Let $x \in \mathbb{R}^d$; the set of projections $\Pi_{\partial\Omega}(x)$ of x onto $\partial\Omega$ is:*

$$\Pi_{\partial\Omega}(x) = \{y \in \partial\Omega, \ \ d(x, \partial\Omega) = |x - y|\}.$$

- *The skeleton Σ of $\partial\Omega$ is the set of points in $\mathbb{R}^d \setminus \partial\Omega$ which have at least two projection points:*

$$\Sigma := \left\{x \in \mathbb{R}^d \setminus \partial\Omega, \ \Pi_{\partial\Omega}(x) \text{ is not a singleton}\right\}.$$

- *When $x \notin \Sigma$, its projection onto $\partial\Omega$ is denoted by $p_{\partial\Omega}(x)$.*

Signed distance function and geometry (II)

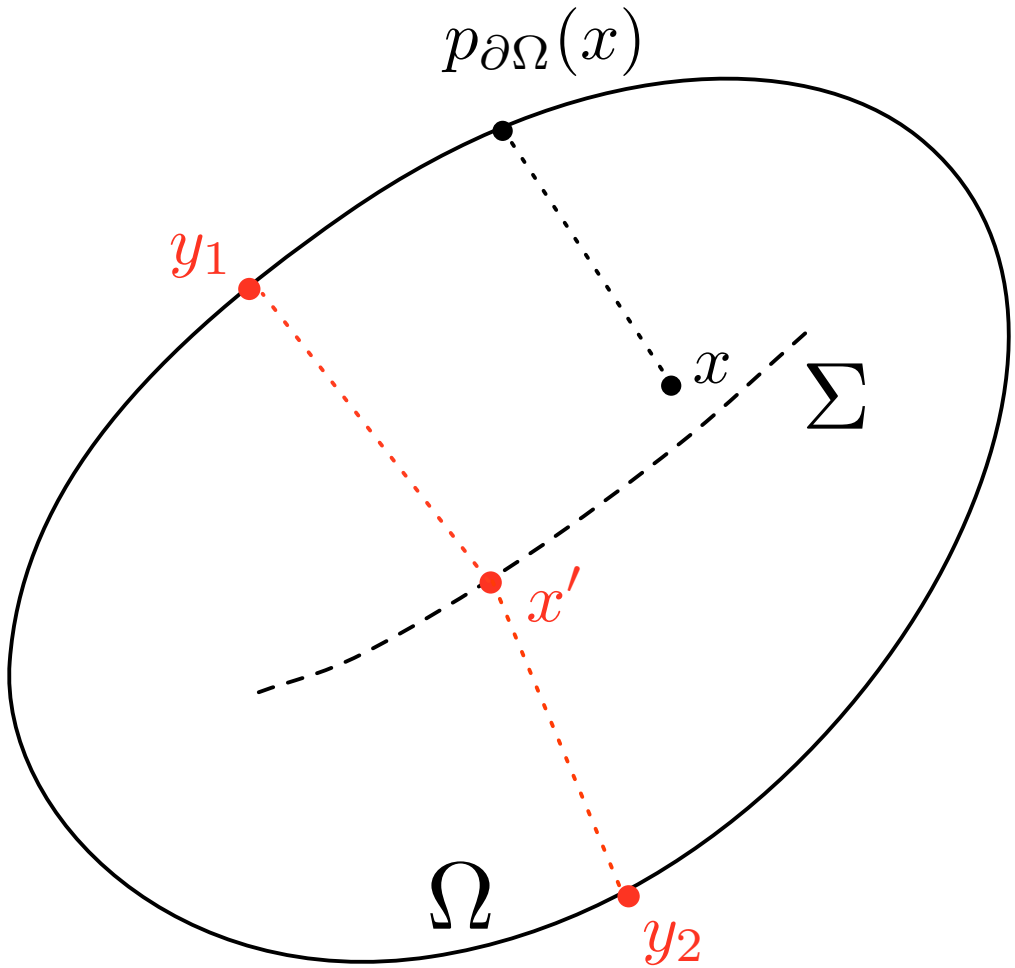

x has a unique projection over $\partial\Omega$, whereas x' has two such points y_1, y_2.

Proposition 3.

Let $\Omega \subset \mathbb{R}^d$ be a Lipschitz, bounded open set;

- *The signed distance function d_Ω is differentiable at every point $x \notin \Sigma$, and its gradient reads:*

$$\nabla d_\Omega(x) = \frac{x - p_{\partial\Omega}(x)}{d_\Omega(x)}.$$

  In particular, $|\nabla d_\Omega(x)| = 1$ wherever it makes sense.

- *If Ω is of class $\mathcal{C}^1$, this last quantity equals $\nabla d_\Omega(x) = n(p_{\partial\Omega}(x))$.*

- *If Ω is of class $\mathcal{C}^k$, $k \geq 2$, then d_Ω is also of class $\mathcal{C}^k$ on a neighborhood of $\partial\Omega$.*

Signed distance function and geometry (IV)

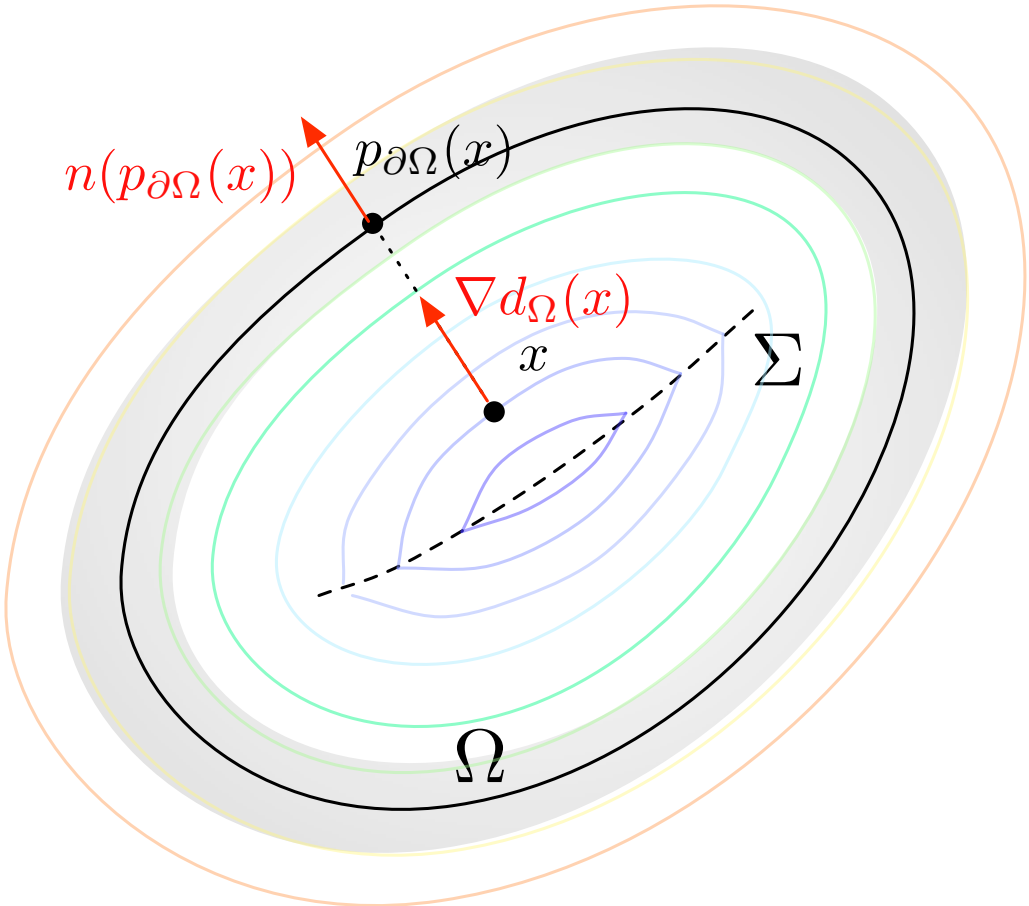

Some level sets of d_Ω are depicted in color; d_Ω is as smooth as the boundary $\partial\Omega$ on the shaded area (at least).

Additional properties of the signed distance function

- The normal vector $n : \partial\Omega \to \mathbb{R}^d$ and a tangential vector field $\tau : \partial\Omega \to \mathbb{R}^d$ are extended to any $x \in \mathbb{R}^d \setminus \Sigma$ by:

$$n(x) \equiv n(p_{\partial\Omega}(x)),$$

and

$$\tau(x) \equiv \tau(p_{\partial\Omega}(x)).$$

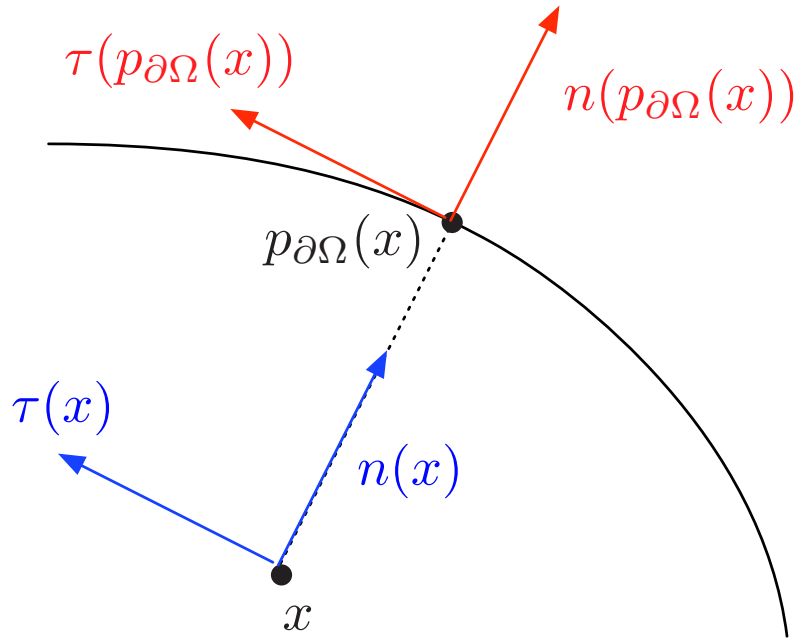

- It is possible to calculate the shape derivative of the signed distance function:

$$\text{For given } x \in \mathbb{R}^d, \ \ \Omega \mapsto d_\Omega(x),$$

and that of integral functionals of the form:

$$\Omega \mapsto \int_D j(d_\Omega)\, dx, \ \text{ where } j : \mathbb{R} \to \mathbb{R}.$$

The 'crust-pattern' model (I)

- The contour of the assembled shape Ω is first printed carefully as a thin crust composed of several offsets of $\partial\Omega$.
- An infill pattern is used for the bulk of Ω: often, rasters of material are deposited with pre-defined orientation and density (air gap between rasters).

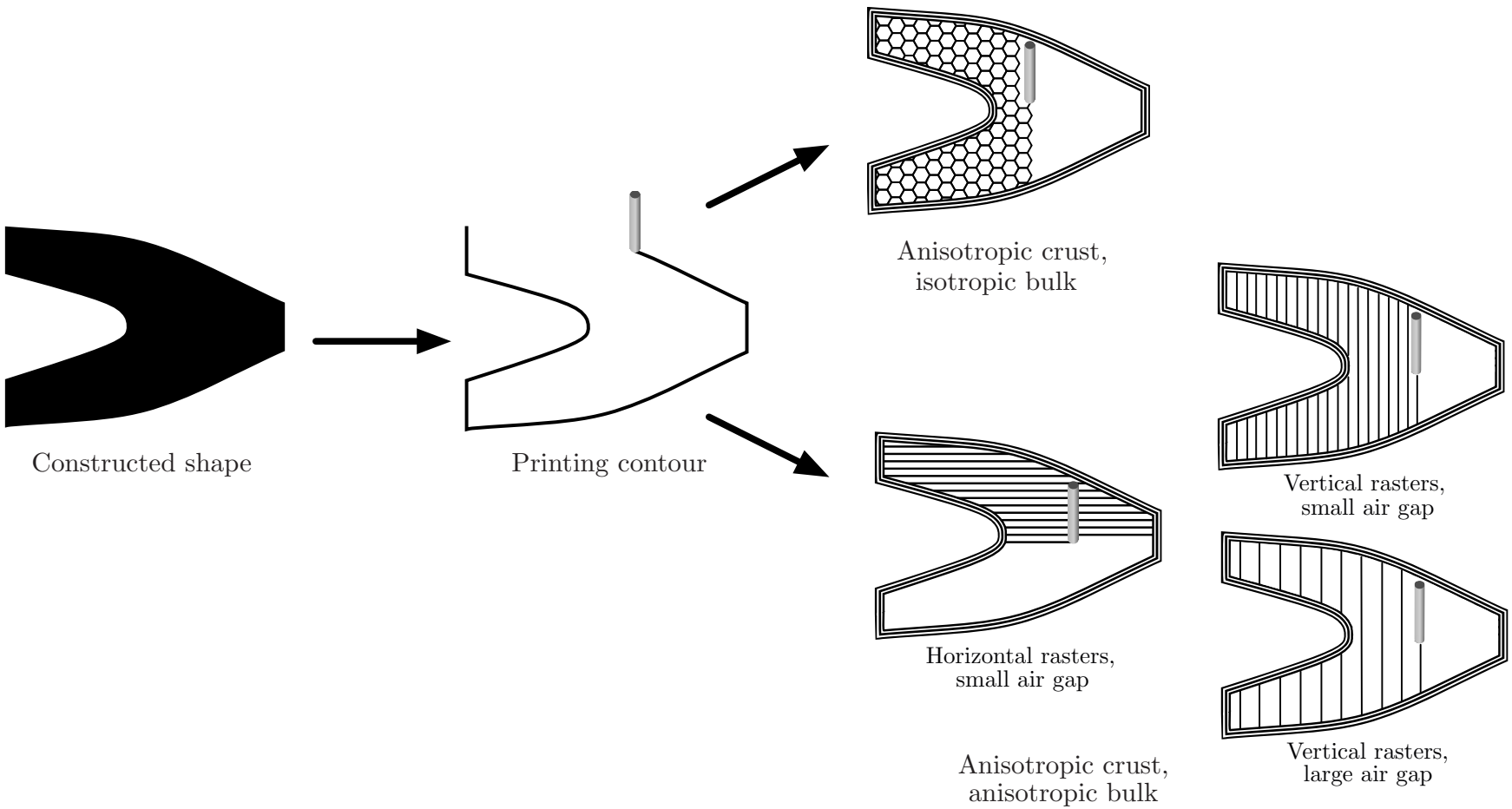

The 'crust-pattern' model (II)

When compared to the expected (isotropic) material properties A_{ref}, the properties A_{Ω}^{cp} of a material printed according to the 'crust-pattern' model are such that:

- In the crust region,
  - The Young's modulus E_τ in the tangential direction is $E_\tau = E_{\text{ref}}$;
  - The Young's modulus E_n in the normal direction is 'weak': $E_n < E_{\text{ref}}$.
- In the infill region,
  - Both $E_{\tau \mathbf{0}}$ and $E_{n\mathbf{0}}$ are proportional to the density ρ of the infill pattern.
  - The Young's modulus is stronger in the direction τ^0 of the rasters than in the transverse direction n^0: $E_{n\mathbf{0}} < E_{\tau \mathbf{0}}$.

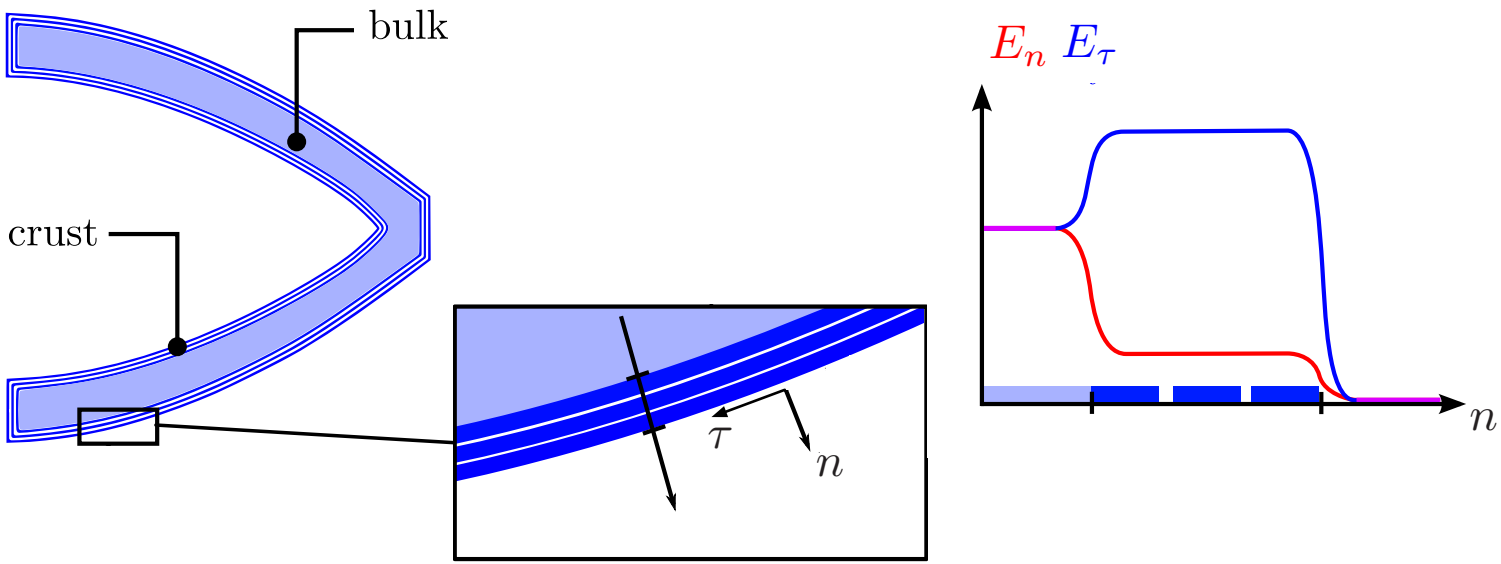

The 'crust-pattern' model (III)

This model relies on a subdivision of the computational domain D into 3 regions:

- The crust $\{x \in D,\ |d_\Omega(x)| < \varepsilon\}$;
- The bulk region $\{x \in D,\ d_\Omega(x) < -\varepsilon\}$;
- The 'void' $\{x \in D,\ d_\Omega(x) > \varepsilon\}$.

The Hooke's tensor $A^{\mathrm{cp}}_\Omega(x)$ reads:

$$\forall x \in D,\ A^{\mathrm{cp}}_\Omega(x) = A^{\mathrm{cp}}(d_\Omega(x), n(x)),$$

where, introducing smooth interpolation functions $h_m,\ h_p : \mathbb{R} \to \mathbb{R}$,

$$A^{\mathrm{cp}}(d,n) = h_m(d)\, A^{\mathrm{cp}}_{\mathrm{bulk}} + (1 - h_m(d) - h_p(d)) A_{\mathrm{crust}}(n) + h_p(d)\, A_{\mathrm{void}}.$$

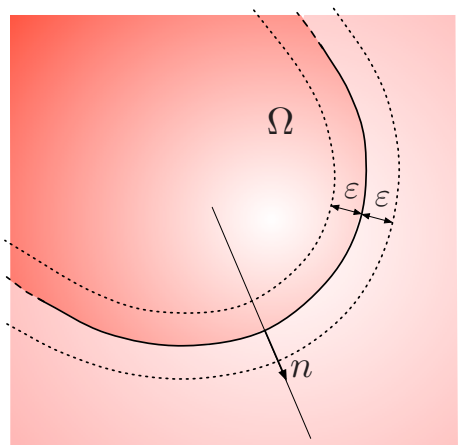

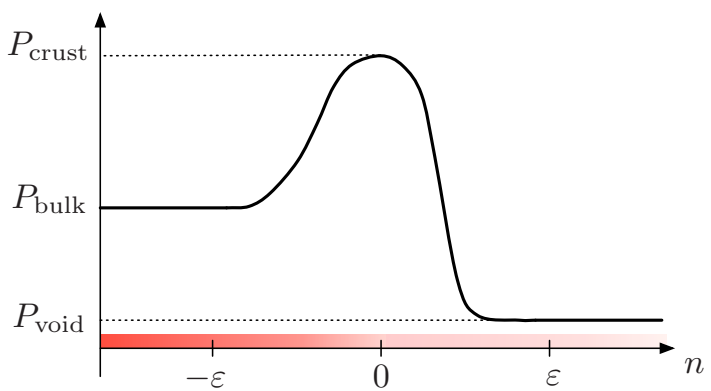

Interpolation of any (scalar) entry P of the tensor A^{cp}_Ω.

The 'offset' model (I)

- The considered 2d layer Ω is printed by following the offsets of the contour $\partial\Omega$ until the core of the layer.
- When compared to the reference material A_{ref}, the properties encoded in the tensor A_{Ω}^{off} are such that:
  - The Young's modulus E_τ in the tangential direction is $E_\tau = E_{\text{ref}}$;
  - The Young's modulus E_n is 'weak' in the normal direction $E_n < E_{\text{ref}}$;
  - All other properties (Poisson's ratios and shear modulus) are those of the reference material.

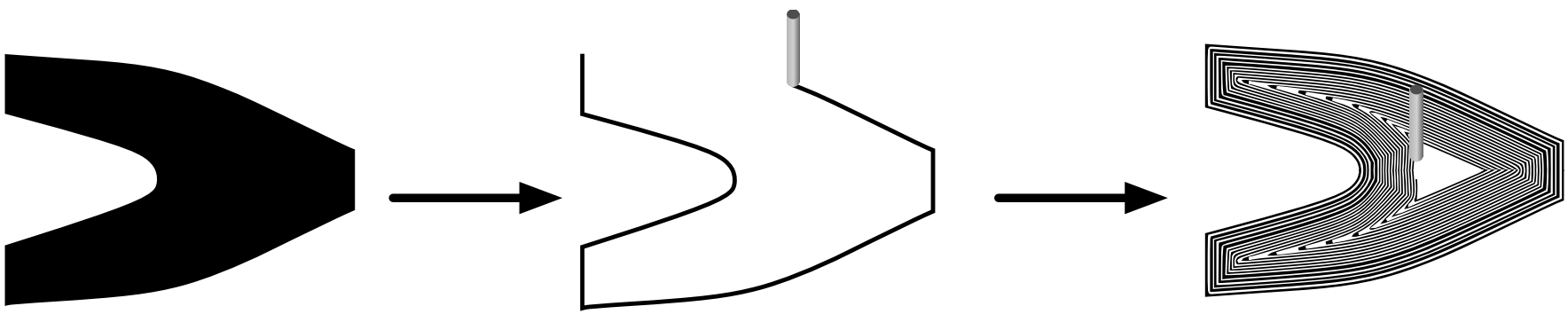

Constructed shape | Printing contour | Offset model

The 'offset' model (II)

In the 'offset model', only two regions of D are considered:

- The shape Ω itself;
- The void $D \setminus \overline{\Omega}$.

The Hooke's tensor $A^{\mathrm{off}}_{\Omega}(x)$ reads:

$$A^{\mathrm{off}}_{\Omega}(x) = A^{\mathrm{off}}(d_{\Omega}(x), n(x)),$$

where, introducing an interpolation profile $h_o : \mathbb{R} \to \mathbb{R}$,

$$A^{\mathrm{off}}(d, n) = h_o(d)\, A^{\mathrm{off}}_{\mathrm{bulk}}(n) + (1 - h_o(d)) A_{\mathrm{void}}.$$

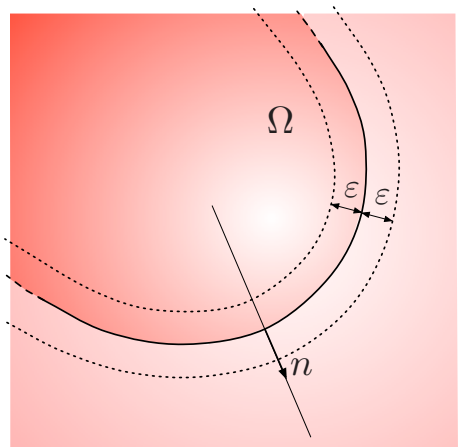

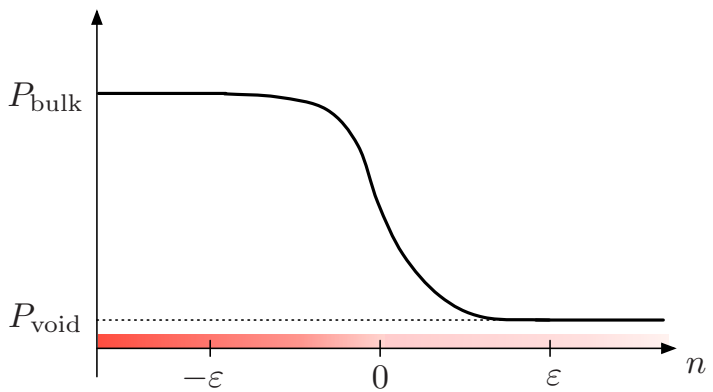

Interpolation of any of the (scalar) entries P of the Hooke's tensor $A^{\mathrm{off}}_{\Omega}$.

Extension to the 3d case

These models extend to the 3d situation by considering an orthotropic Hooke's tensor with weak rigidity (i.e. Young's modulus) in the build direction.

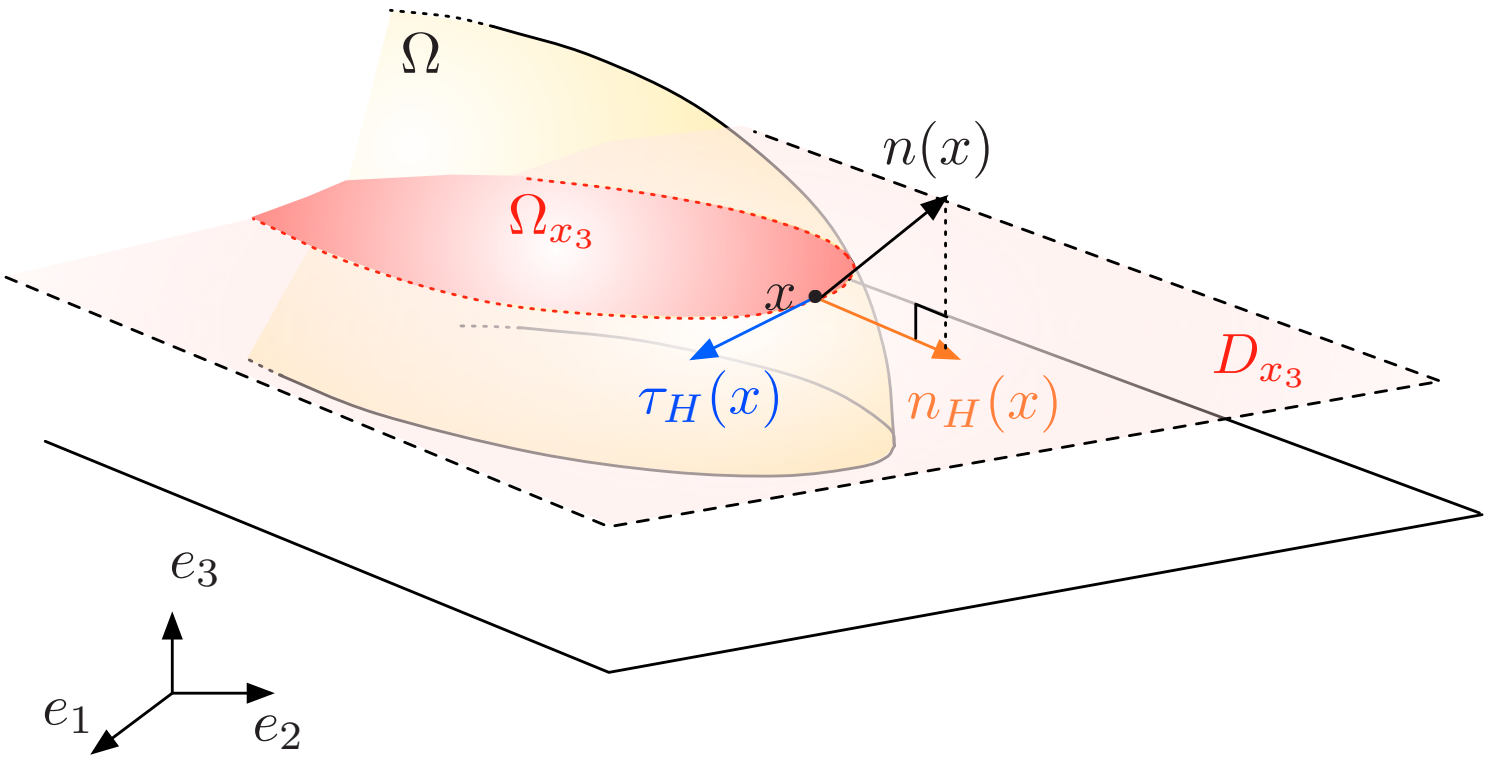

In three space dimensions, the natural frame for the orthotropy of the material in the crust region is (τ_H, n_H, e_3).

Shape derivative

We consider a generic Hooke's tensor of the form:

$$A_\Omega(x) = A(d_\Omega(x), n(x)), \text{ for some mapping } A : \mathbb{R}_s \times \mathbb{R}_n^d \to \mathcal{L}(\mathbb{S}_d(\mathbb{R}), \mathbb{S}_d(\mathbb{R})).$$

Theorem 4.

The compliance

$$J(\Omega) = \int_D A_\Omega e(u_\Omega) : e(u_\Omega)\, ds$$

is shape differentiable at $\Omega \in \mathcal{U}_{\mathrm{ad}}$ and its shape derivative reads:

$$\begin{aligned} J'(\Omega)(\theta) = \quad & \int_\Gamma \left(\int_{\mathrm{ray}_{\partial\Omega}(x)} q_\Omega(x, d_\Omega(z)) \left(\frac{\partial A}{\partial s}(d_\Omega, n) e(u_\Omega) : e(u_\Omega) \right)(z)\, d\ell(z) \right) (\theta \cdot n)(x)\, ds(x) \\ & - \int_\Gamma \mathrm{div}_{\partial\Omega} \left(\int_{\mathrm{ray}_{\partial\Omega}(x)} Q_\Omega(x, d_\Omega(z)) \left(\frac{\partial A}{\partial n}(d_\Omega, n) e(u) : e(u) \right)(z)\, d\ell(z) \right) (\theta \cdot n)(x) ds(x) \\ & + \int_\Gamma \left(\int_{\mathrm{ray}_{\partial\Omega}(x)} Q_\Omega(x, d_\Omega(z)) \left(\frac{\partial A}{\partial n}(d_\Omega, n) e(u) : e(u) \right)(z)\, d\ell(z) \right) \cdot n\, \kappa(x)(\theta \cdot n)(x)\, ds(x), \end{aligned}$$

where $\mathrm{div}_{\partial\Omega} v := \mathrm{div} v - (\nabla v n) \cdot n$ is the tangential divergence of a smooth vector field $v : \partial\Omega \to \mathbb{R}^d$, and the quantities $q_\Omega(x, s)$ and $Q_\Omega(x, s)$ are defined by:

$$q_\Omega(x, s) = \prod_{i=1}^{d-1} (1 + s\kappa_i(x)), \text{ and } Q_\Omega(x, s) = -\mathrm{I} + s\mathrm{II}_\Omega(x)(\mathrm{I} + s\mathrm{II}_\Omega(x))^{-1}.$$

The cantilever, considering different printing patterns (I)

We consider the two-dimensional cantilever example.

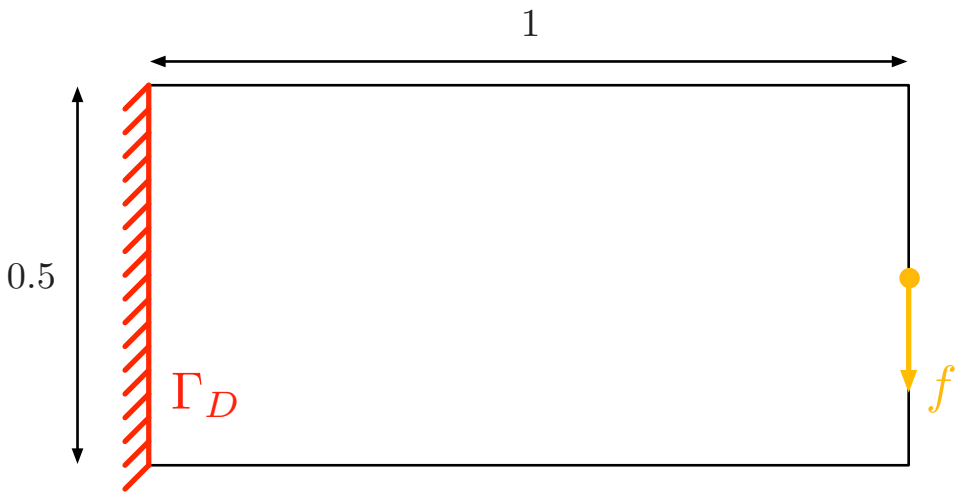

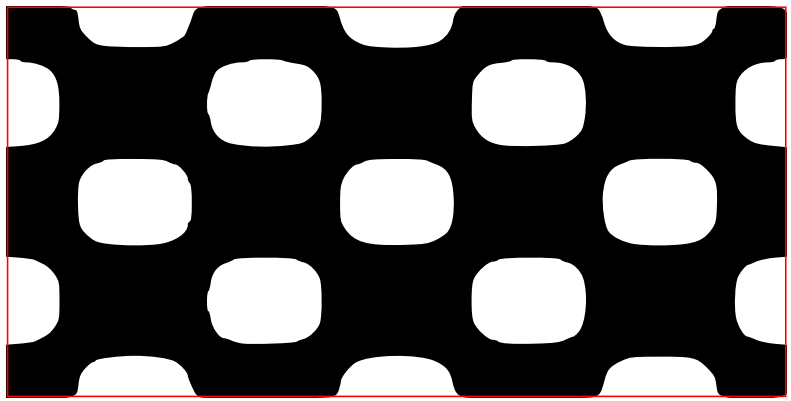

(Left) Setting and (right) initial design in the cantilever test case.

We minimize the volume of the structure:

$$\begin{aligned} \min_{\Omega} \quad & \mathrm{Vol}(\Omega), \\ \text{s.t.} \quad & C(\Omega) \leq \alpha_c \end{aligned}$$

The cantilever, considering different printing patterns (II)

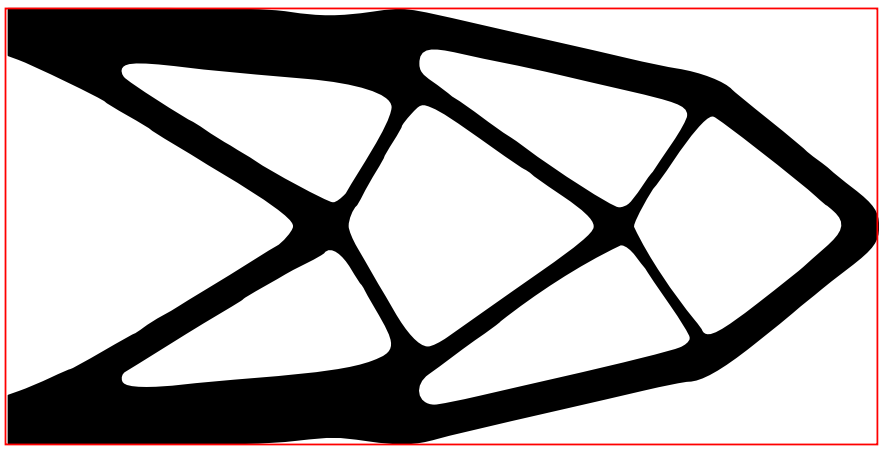

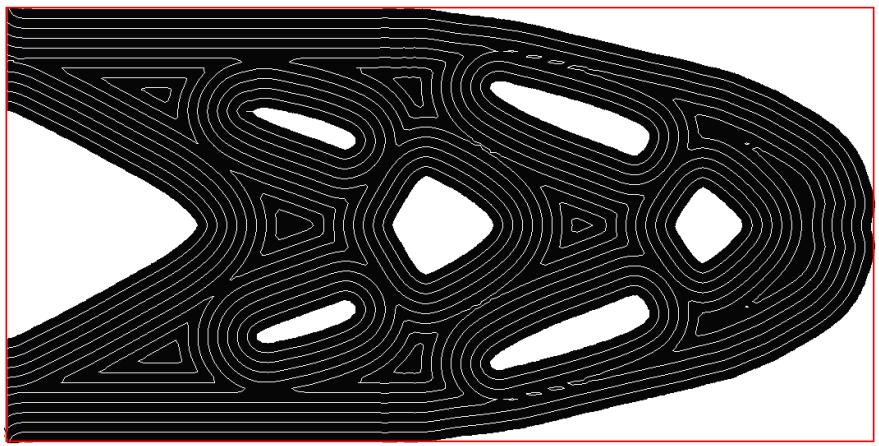

Optimized 2d cantilevers in (left) the 'molded' case, and (right) the 'offset' model.

The cantilever, considering different printing patterns (III)

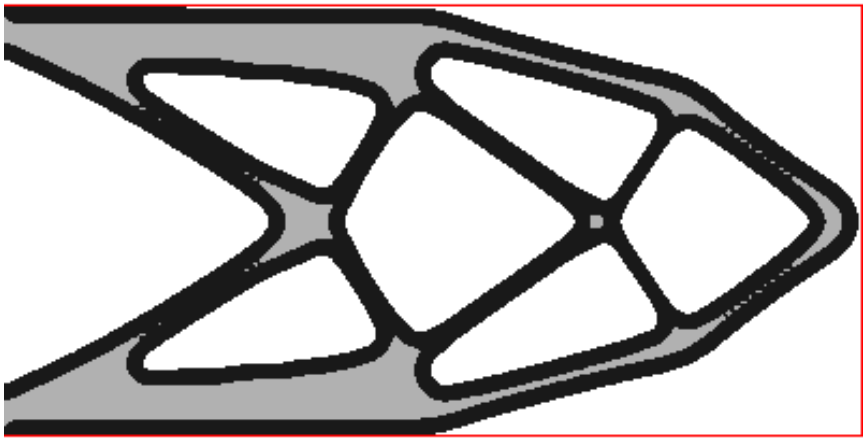

(c) isotropic crust and infill

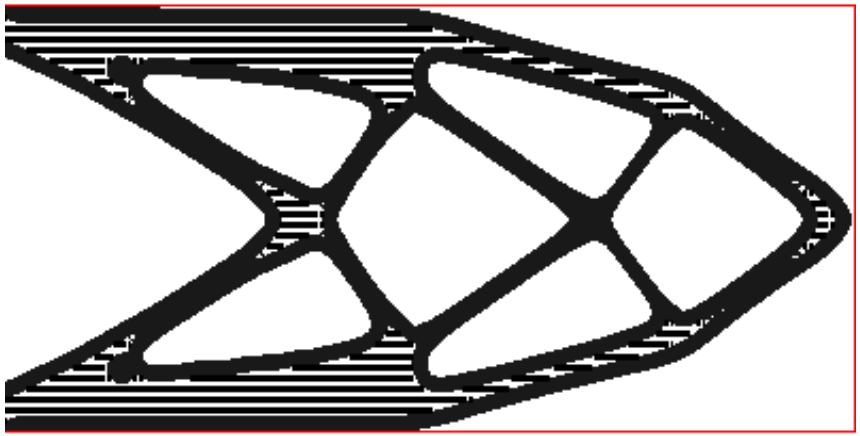

(d) isotropic crust and anisotropic infill

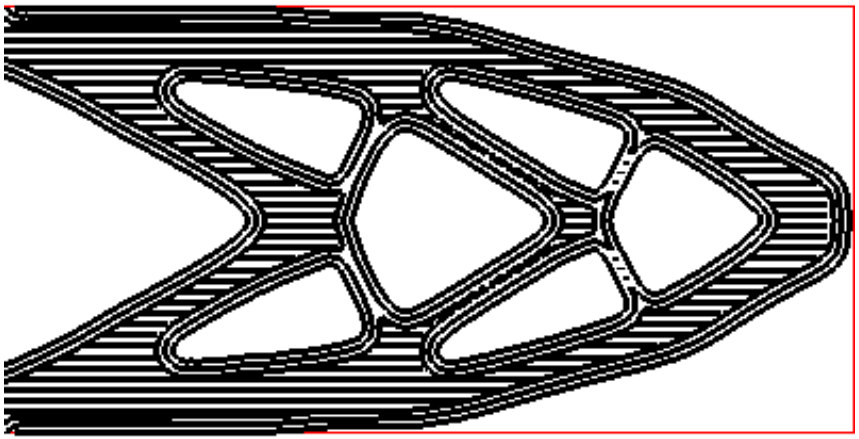

(e) anisotropic crust and infill

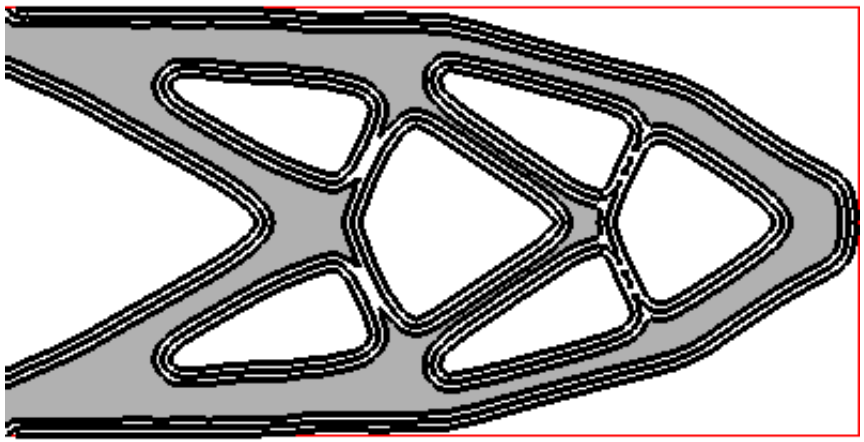

(f) anisotropic crust and isotropic infill

Optimized shapes in the cantilever example obtained with the four 'crust-pattern' models considered for the assembly of shapes, using an infill density $\rho^{\mathrm{cp}}_{\mathrm{bulk}} = 0.90$.

The cantilever, considering different printing patterns (IV)

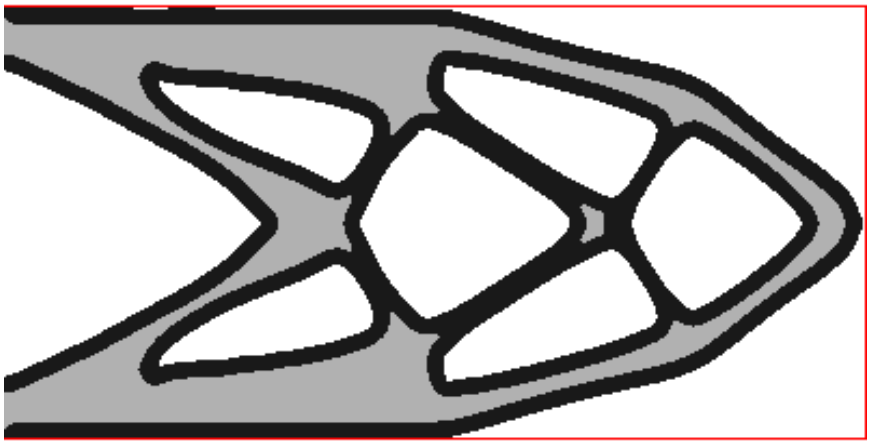

(c) isotropic crust and infill

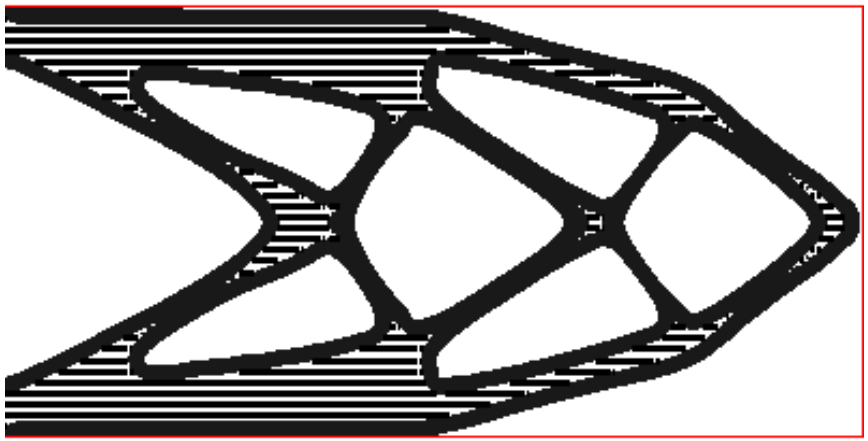

(d) isotropic crust and anisotropic infill

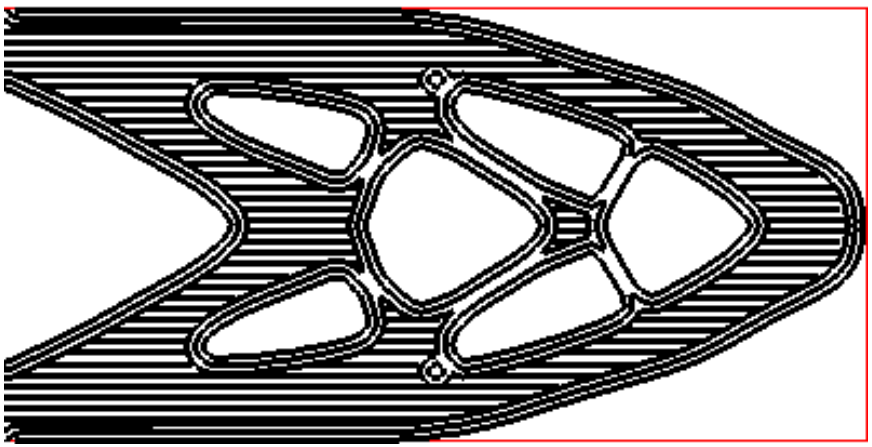

(e) anisotropic crust and infill

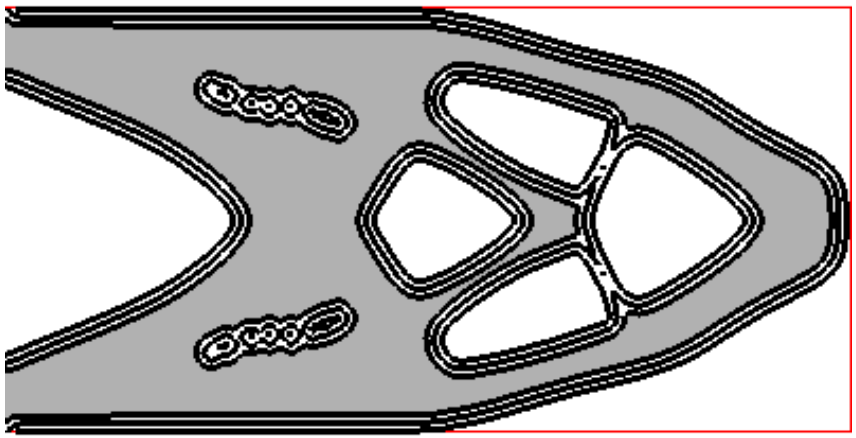

(f) anisotropic crust and isotropic infill

Optimized shapes in the cantilever example obtained with the four 'crust-pattern' models considered for the assembly of shapes, using an infill density $\rho^{\mathrm{cp}}_{\mathrm{bulk}} = 0.75$.

The cantilever, considering different printing patterns (V)

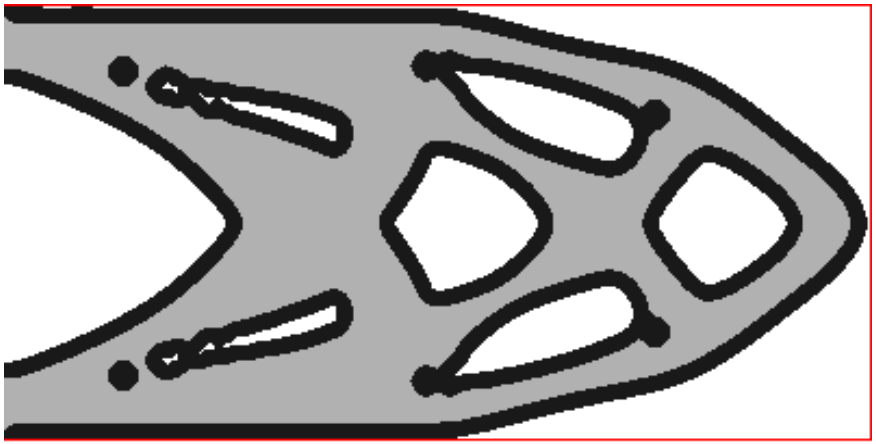

(c) isotropic crust and infill

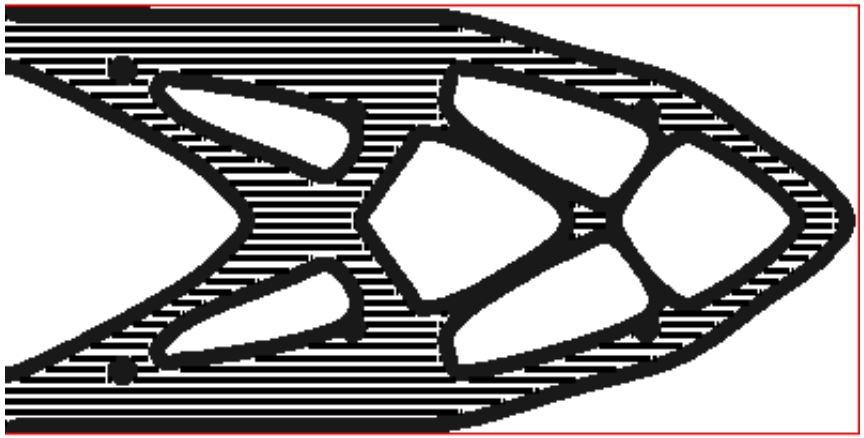

(d) isotropic crust and anisotropic infill

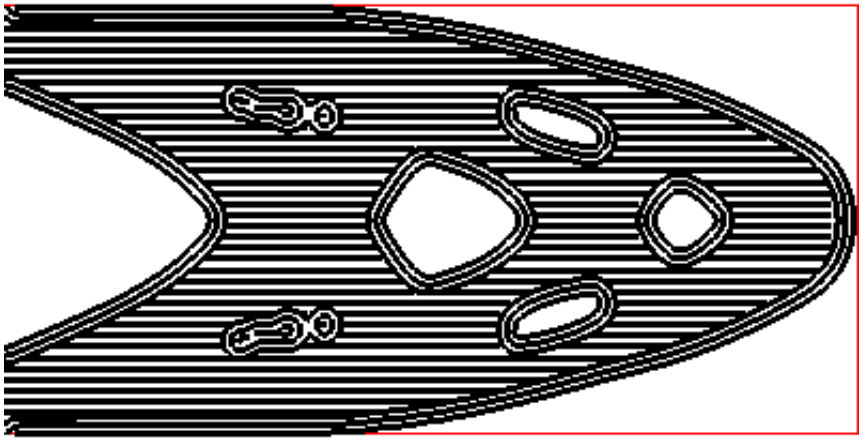

(e) anisotropic crust and infill

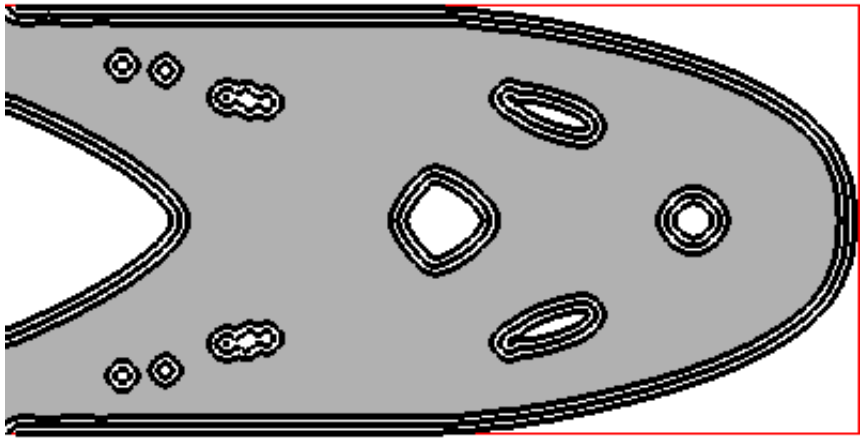

(f) anisotropic crust and isotropic infill

Optimized shapes in the cantilever example obtained with the four 'crust-pattern' models considered for the assembly of shapes, using an infill density $\rho^{\mathrm{cp}}_{\mathrm{bulk}} = 0.60$.

The MBB beam, considering different printing patterns (I)

We now turn to the two-dimensional MBB beam example.

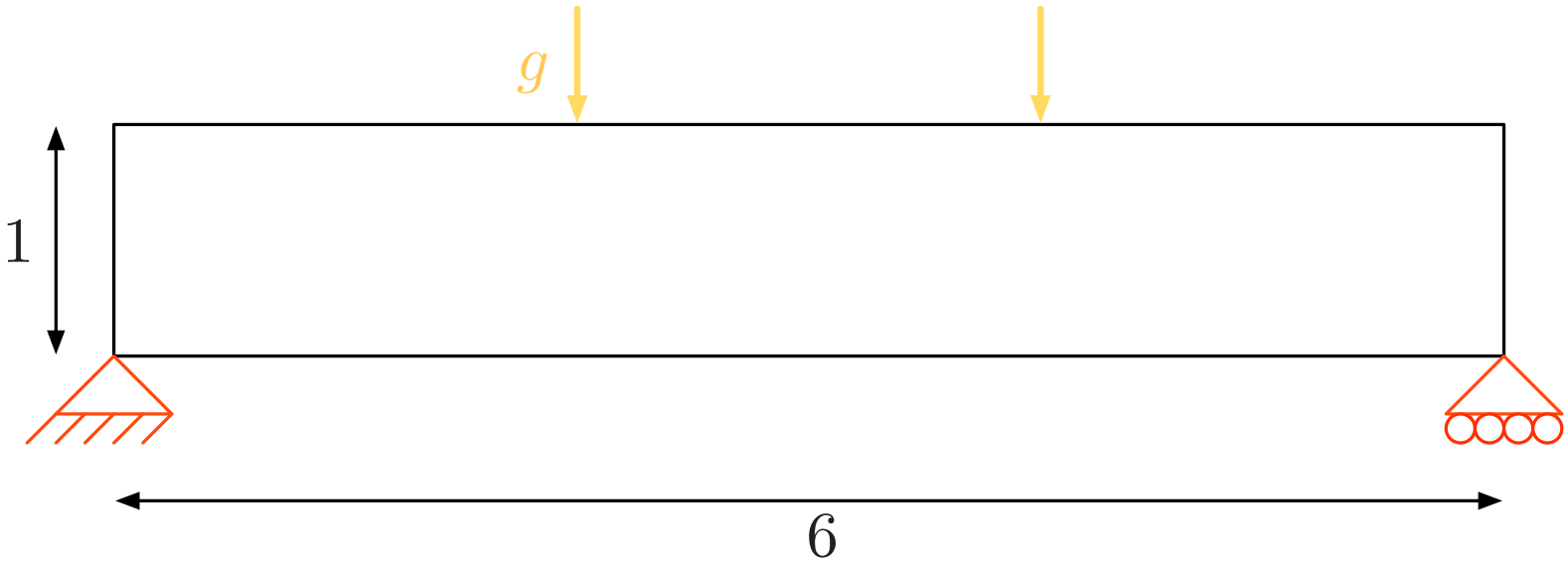

Setting of the MBB beam test case.

Again, we minimize the volume of the structure:

$$\begin{aligned} \min_{\Omega} \quad & \mathrm{Vol}(\Omega), \\ \text{s.t.} \quad & C(\Omega) \leq \alpha_c \end{aligned}$$

The MBB beam, considering different printing patterns (II)

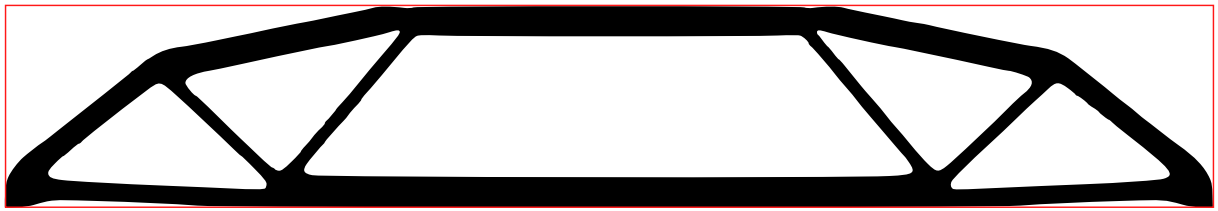

(a) 'Molded' situation

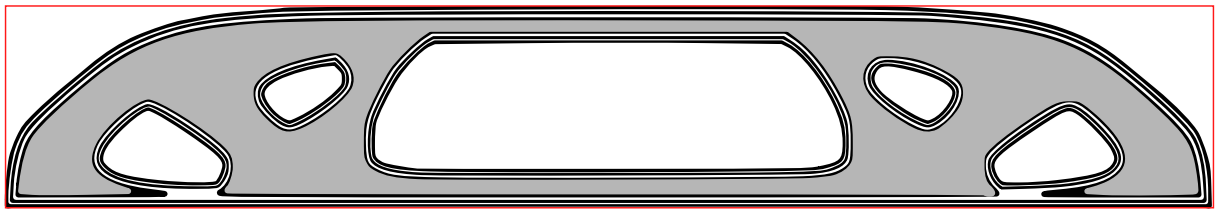

(b) 'Crust-pattern' model with anisotropic crust, isotropic bulk

(c) 'Crust-pattern' model with isotropic crust, isotropic bulk

(d) 'Crust-pattern' model with isotropic crust, anisotropic bulk with horizontal rasters

Thank you !

Thank you for your attention!

References I

[AlDaFauMiEs] G. Allaire, C. Dapogny, A. Faure, G. Michailidis and R. Estevez, *Shape optimization of a layer by layer mechanical constraint for additive manufacturing*, C. R. Math. Acad. Sci. Paris, 355, (2017), pp. 699-717.

[AlDaFauMiEs2] G. Allaire, C. Dapogny, A. Faure, G. Michailidis and R. Estevez, *Structural optimization under overhang constraints imposed by additive manufacturing technologies*, J. Comput. Phys., 351, (2017), pp. 295-328.

[AlJak] G. Allaire, L. Jakabcin, *Taking into account thermal residual stresses in topology optimization of structures built by additive manufacturing*, Math. Models and Methods in Applied Sciences, 28(12), (2018), pp. 2313-2366.

[AlJouToa] G. Allaire and F. Jouve and A.M. Toader, *Structural optimization using shape sensitivity analysis and a level-set method*, J. Comput. Phys., 194 (2004) pp. 363–393.

[CheLuChou] B. Cheng, P. Lu and K. Chou, *Thermomechanical Investigation of Overhang Fabrications In Electron Beam Additive Manufacturing*, ASME 2014 International Manufacturing Science and Engineering Conference, (2014).

References II

[DaFauMiEs2] C. Dapogny, R. Estevez, A. Faure and G. Michailidis, *Shape and topology optimization considering anisotropic features induced by additive manufacturing processes*, Comput. Meths. Appl. Mech. Engrg., 344, (2019), pp. 626–665.

[DuHeLe] J. Dumas, J. Hergel and S. Lefebvre, *Bridging the Gap: Automated Steady Scaffoldings for 3D Printing*, ACM Trans. Graph., 33, 4, (2014), pp. 1–10.

[GiRoStu] I. Gibson, D.W. Rosen and B. Stucker, *Additive manufacturing technology: rapid prototyping to direct digital manufacturing*, Springer Science Business Media, Inc, (2010).